# ACOUSTIC BACKSCATTER FROM PHYTOPLANKTON

by

Dylan Lucien DeGrâce

Submitted in partial fulfillment of the requirements
for the degree of Master of Science

at

Dalhousie University
Halifax, Nova Scotia
December 2018

*To my loving partner, my family, and my pup. Thank you for all of your support along the way. You guided me to the light at the end of the tunnel.*

# TABLE OF CONTENTS

# LIST OF TABLES

# LIST OF FIGURES

# ABSTRACT

Methods for the detection and monitoring of phytoplankton are often limited by low temporal and spatial resolution. The use of a high-frequency broadband acoustic system could provide improvements both temporally and spatially, and would be especially advantageous when used in conjunction with methods that provide taxonomic information. With this motivation, a high-frequency broadband active acoustic system has been developed and used in four laboratory trials to observe the backscatter from four morphologically-distinct species of phytoplankton whose sizes range from approximately 10 to $100\,\mu\mathrm{m}$. The cultures were insonified at frequencies between 0.75 MHz and 6.9 MHz, using three broadband transducers (with center frequencies of 1, 2.25, and 5 MHz.) Two of the species were detected with confidence and the concentration detection limits for these two species are proposed. Volume scattering strength spectra for each species are compared with the best-fit scattering models drawn from the zooplankton scattering literature and this is used to suggest probable organism composition and the best options for modelling the scattering from these species. The potential for an acoustic phytoplankton species-detection and monitoring system is discussed.

# ACKNOWLEDGEMENTS

First and foremost, I must thank my (officially, co-) supervisor Tetjana Ross for her unwavering support and commitment to see this thesis through to its end including the many suggestions, edits, re-edits, and overall guidance. To Alex Hay, who filled the role as co-supervisor when Tetjana moved west and for his commitment and experience that was essential to many parts of this thesis; thanks for the many desk-side chats, I learned a great deal. And to Hugh MacIntyre who I am indebted to for nearly everything biology-related in this thesis. Thanks to David Barclay for agreeing to take part in my defence.

Special thanks to Hugh's lab team, especially Shannah Rastin and Jessica Miller, for their expertise in growing and maintaining phytoplankton cultures; you were no doubt essential to this thesis. To Mark Merrimen for his role in the designing and construction of the testing apparatus.

To the Oceanography Department and all its members. Thank you for making my choice to pursue oceanography an unregrettable one. To Dan Kelley for the lessons in-class and out, your friendliness, and candid nature; it was always a pleasure to chat with you. To Richard Cheel, my office neighbour, for our enjoyable hour-long chats about nothing of importance to your guidance on programming and scientific problems. And to my peers, especially Nick Dourado, Gennavieve Ruckdeschel, Jenna Hare, and Tristan Guest, thank you for your friendship and help throughout this thesis.

Most significantly, to my partner, family, and close friends from the East Coast to West. Thank you for your endless love and support. I would not have been able to finish this thesis without it.

This research was made possible by funding from the Nova Scotia Innovation and Research Graduate Scholarship (NSIRGS) and the Natural Sciences and Engineering Research Council of Canada (NSERC). Thank you for the opportunity.

# CHAPTER 1

# INTRODUCTION AND BACKGROUND

## 1.1 Research Motivation

Phytoplankton, at the base of the food web, play an essential role in marine, coastal and lacustrine environments. They are small and numerous, perform a large share of the primary production and, subsequently, are excellent indicators of ecological variation (*Paerl et al.*, 2007).

As a key example, over-enrichment of nutrients (especially nitrogen) increases the formation of harmful algal blooms (HABs). The HABs strongly influence the productivity, water quality, biodiversity and overall ecosystem health within the affected marine and freshwater systems (*Conley*, 2000; *Cloern*, 2001; *Rabalais and Turner*, 2001). Harmful algal blooms pose further risk when species containing toxins enter our drinking water or food supply. In recent years it has been found that the occurrence of HABs is increasing (*Rabalais et al.*, 2009). An example of an algal bloom is shown in Figure 1.1 where a toxic species, *Microcystis aeruginosa*, bloomed in October, 2011; highlighting the large scale and influence that HABs can have.

With the human health risks associated with HABs and the importance of phytoplankton to marine food webs, it is vital to monitor phytoplankton. A variety of monitoring techniques are already used, ranging from laboratory methods such as flow cytometry and microscopy to remote sensing methods such as satellite optics (*Platt and Sathyendranath*,

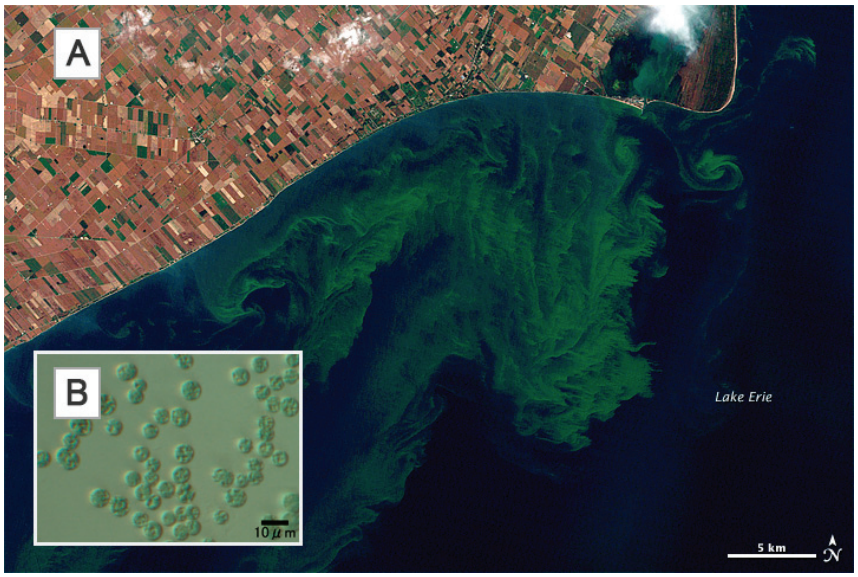


Figure 1.1: Example of a *Microcystis aeruginosa* bloom in Lake Erie. (A) A *Microcystis aeruginosa* bloom along the western banks of Lake Erie on October 5, 2011 (*NASA Earth Observatory*). (B, inset) Microscopic image of *M. aeruginosa* (*Algae Resource Database*).

2008). These current detection methods are capable of producing accurate results but are not without limitations.

Laboratory methods in current use are both time consuming and can lack the temporal resolution necessary for monitoring the rapid growth of HABs. And, while they can provide good temporal resolution and horizontal coverage, satellite remote sensing methods cannot observe HABs at depths larger than a few meters due to high light attenuation. Additionally, interpreting satellite optical data in terms of phytoplankton is challenging in coastal environments for a number of reasons; e.g. their limited spatial resolution and elevated levels of colored dissolved organic material which further increases light attenuation. It is also these coastal areas that are more prone to HABs, further necessitating their monitoring. A potential alternative approach is to use high-frequency acoustic backscatter techniques. These acoustic techniques can provide full water column, high temporal resolution monitoring in both coastal areas and regions further off-shore.

This thesis explores the possibility of using an active broadband acoustic system to, firstly, detect phytoplankton with sufficient accuracy and then suggest if classification

is possible. If successful, a similar system could be further developed and deployed in order to monitor species in the field with the intention of capturing the early onset of rapid growth that HABs exhibit. In general, the thesis builds on the wealth of existing literature on the study of zooplankton using high frequency broadband acoustic systems and works to apply many of the same techniques in the study of phytoplankton.

However, phytoplankton provide their own set of challenges. Namely, they are smaller than zooplankton and are likely to be weaker scatterers (even those species with thicker shells) and will require a careful application of the experimental methods described in zooplankton literature. Previous studies into the acoustic backscatter of phytoplankton are limited and did not incorporate the more contemporary techniques that have been developed in zooplankton studies. This thesis hopes to bridge this gap and provide a more thorough study of the backscatter from and the potential for classification of exemplar phytoplankton species.

## 1.2 Background

### 1.2.1 High-Frequency Acoustics

High-frequency acoustic backscatter has long been used to locate and quantify the abundance of small scale (millimeters or less) objects (e.g. zooplankton: *Greenlaw* (1979); *Holliday et al.* (1979); *Martin et al.* (1996)) and phenomena (e.g. microstructure mixing events: *Ross and Lueck* (2003)) within the ocean. Through the use of active acoustics, high temporal resolution is easily achieved. Most importantly, sound is much less attenuated than light in water and allows for the detection of particles such as phytoplankton at depth.

Active acoustic systems consist of both transmitting and receiving components. The temporal resolution is limited only by how frequently the system transmits (i.e. pings), which is in turn limited by the range over which the observations need to be made.

In using a continuous broadband acoustic system, scattering information is provided at a wide range of acoustic frequencies, providing a significant analytic advantage over

single-frequency or narrowband systems – and is especially advantageous when performing an initial comparative analysis as is the goal of this thesis. By using pulse compression (or matched filtering) techniques (*Chu and Stanton*, 1998), the bandwidth of a broadband system also improves range resolution, providing an additional advantage over any similar narrowband system.

For each ping, there are several important factors that affect the propagation of a sound wave through water: geometric spreading, absorption, and scattering. Geometric spreading is independent of frequency and depends on the geometry of the system – causing the sound level to decrease as the distance to the source increases. Absorption, in general, increases with frequency and depends on the water properties (*Francois and Garrison*, 1982, Fig. 8). Acoustic scattering will occur when there is any variation in the medium's density or sound speed contrast – a larger contrast produces more scatter. Backscatter refers to sound that scatters 180° ($\pi$ radians) relative to its initial propagation; i.e. *back* towards the transmitter. In addition to density and sound speed contrasts, scattering is dependent on the relationship between the size of a scatterer ($a$) and the acoustic wavelength ($\lambda$). The *Rayleigh scattering* regime is defined where $\lambda \gg a$ and results in scattering that is proportional to only the scatterer size relative to the wavelength for a given speed and density contrast. *Geometric scattering* is defined where $\lambda \ll a$ and scattering is now proportional to morphology and orientation in addition to size, speed contrast and density contrast.

Ideally, for the purpose of species identification, the geometric and geometric-to-Rayleigh transition (i.e. $\lambda \approx a$) regimes would provide the most promising test ranges. This imposes a weak threshold on usable frequencies between 2 and 20 MHz when working with species at the 10 to $100\,\mu\mathrm{m}$ scale. However, because of instrument limitation, the experiments in this thesis were only able to reach the lower bound of the transition region. While this limits the feasibility in species identification, it can provide a good initial description of the scattering mechanisms of the test species. Near this scale, bioacoustics

has been highly successful when studying zooplankton (*Holliday et al.*, 1979; *Stanton et al.*, 1994, 2000; *Lavery et al.*, 2007) and the few studies with phytoplankton have been successful enough to warrant further investigation (*Selivanovsky et al.*, 1996; *Blanc et al.*, 2000; *Kim et al.*, 2010).

### 1.2.2 Acoustic Studies of Zooplankton & Phytoplankton

Applying acoustic techniques to the study of zooplankton has grown in popularity over the last 40 years whose foundations are the studies by *Greenlaw* (1979); *Holliday et al.* (1979) and later by *Stanton et al.* (1987). Prior to these studies, using acoustics was prevalent in the detection and quantification of fish populations–a task more easily accomplished owing to their size and the markedly strong scatter of their swim bladders. However, challenges in observing zooplankton are not limited to their size.

Within zooplankton populations, features such as morphology (i.e. shape), structure (e.g. shells), and size can vary considerably (*Stanton et al.*, 1994). Even populations of the same size produce drastically different scattering due to variation in their morphology and structure. Accurately detecting and classifying zooplankton populations therefore requires appropriately defined models based on the primary scattering mechanism and good estimates of the organism's density contrast ($g$) and sound speed contrast ($h$) relative to the water. Figure 1.2 illustrates the variability possible from different models. A primary research question has dealt with applying the most appropriate acoustic scattering model for a given zooplankter morphology. *Stanton et al.* (1994) categorized zooplankton into three different groups based on their primary scattering mechanisms: 1) weakly scattering and fluid-like, 2) those with gas inclusions and 3) and those with hard-elastic shells.

Weakly scattering fluid-like zooplankton are perhaps the most straight-forward and were studied prior to Stanton's categorization (*Greenlaw*, 1979; *Holliday et al.*, 1979). These studies successfully applied fluid-sphere models (*Anderson*, 1950) to scattering by copepods. Modifications to the fluid-sphere models such as the deformed cylinder model (*Stanton*, 1989) were subsequently applied by *Stanton et al.* (1994) to scattering by krill

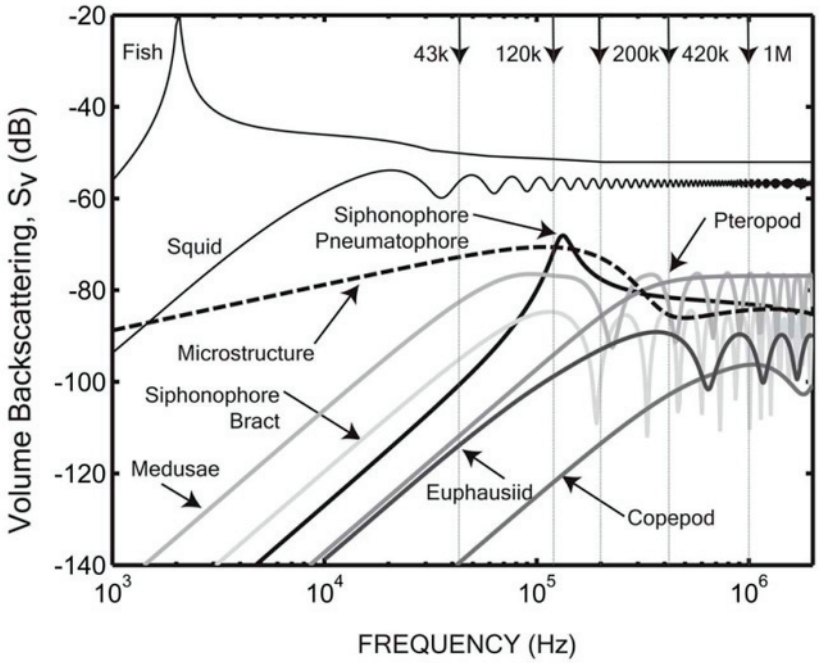


Figure 1.2: Example of the variability in different scattering models (*Lavery et al.*, 2007, fig. 1). See reference for model parameters.

and salps. *Stanton et al.* (1994) also used the fluid model when studying zooplankton containing gas-inclusions–in this case, the body is neglected because of the considerably higher scatter from the strongly contrasting gas-inclusion. The model describing fluid-like zooplankton was again improved with the introduction of the distorted-wave Born approximation (DWBA) (*Stanton et al.*, 1998b). With the DWBA models, shapes are no longer restricted to simple geometry and can take on complex features. An additional strength is that all orientations of the organism can be modeled, whereas before most studies only modeled broadside incidence (*Stanton et al.*, 1998b).

Modeling scatter from hard-elastic shelled zooplankton originally made use of a modified fluid-sphere model (*Johnson*, 1977) valid only for smaller acoustic wavelengths relative to organism size (or, higher acoustic frequencies). *Stanton* (1989) expanded this theory to include other shapes such as a spheroid and a uniformly-bent cylinder and subsequently applied it to gastropods (*Stanton et al.*, 1994). A solution viable for all frequencies was later applied by *Stanton et al.* (2000) and expands on theory for fluid-filled

elastic shell scatters (*Goodman*, 1962).

The studies discussed so far have primarily focused on the forward problem: predicting scattering from known morphologies. Recently, the inverse problem has been the focus of study (*Martin et al.*, 1996; *Lavery et al.*, 2007). Application of the inverse scattering problem is challenging as a robust understanding of the forward scattering problem must first be achieved. *Lavery et al.* (2007) was able to show that abundance measurements of the smaller, more abundant, and less mobile zooplankton were in good agreement with traditional techniques (e.g. net haul samples).

In contrast to zooplankton, research on acoustic scattering from phytoplankton is very limited. The literature is restricted to five peer-reviewed articles (*Selivanovsky et al.*, 1996; *Blanc et al.*, 2000; *Kim et al.*, 2010, 2017, 2018). In these articles the authors tested the feasibility of phytoplankton detection with acoustics. *Selivanovsky et al.* (1996) had very limited data and focused on gas-filled cavities of some species as the main scattering mechanism. In a more conclusive study, a phytoplankton biomass was estimated from lab-grown cultures using single-frequency insonification (*Blanc et al.*, 2000). *Kim et al.* (2010), using a chain-forming species that commonly form blooms in the near-shore waters, estimated density and sound speed contrasts of the organism from samples collected in the field, using a simple model. These last two papers served as some of the primary motivation at the start this thesis. In addition, however, during the course of my experiments, two other articles were released: *Kim et al.* (2017) and *Kim et al.* (2018) use high-frequency acoustic systems to measure backscattering from phytoplankton both in the laboratory and in the field, but still only use single-frequency acoustics and assume simple scattering models.

*Selivanovsky et al.* (1996) primarily investigated the scattering from gas-filled cavities (vacuoles) within different phytoplankton species. Using frequencies between 2 and 11 MHz they were able to weakly confirm that an increased presence of gas cavities increases the target strength of cells. They were unable to draw strong conclusions due

to limitations in their methods. Therefore, the work by *Blanc et al.* (2000) and *Kim et al.* (2010) holds more promise as a model and motivation for this study.

*Blanc et al.* (2000) worked with *Skeletonema costatum*, a diatom that often dominates surface waters in coastal areas. In their setup, a single frequency of 2.6 MHz insonified *S. costatum* cultures while they were growing in the lab. A modified fluid-sphere scattering model was used in order to predict scattering volume (as recommended by *Holliday et al.* (1979)). The modifications were done to account for the elastic shell as a primary scatterering mechanism. Curiously, they did not consider the model for an elastic-shelled scatterer. Estimates of the density and sound speed contrasts were taken from literature paying special attention to the diatom shell influence (*Blanc et al.*, 2000). This highlights an important limitation of single frequency insonification. Without data spanning multiple frequencies, the effects of $g$ and $h$ (in addition to size and morphology) are confounded as a single factor. Determining these values independently can be aided with the use of broadband acoustics. Despite this limitation, their method was able to produce a reasonable estimate, by inspection (no regression statistics are shown), of *S. costatum* concentration.

*Kim et al.* (2010) studied acoustic scattering from the toxic, chain-forming, species *Cochlodinium polykrikoides*, which is prone to bloom in Korean coastal waters. Samples with varying concentrations were collected from field locations during a bloom and taken back to the lab for acoustic study. Insonification was done at a single frequency, this time at 5 MHz. The cell chains were modeled by calculating for an equivalent spherical diameter to represent the entire chain length. These model predictions correlated well with the backscatter results, producing values for $g$ and $h$ similar to the literature (1.07 and 1.06 respectively) – again taking note of the single frequency limitation discussed earlier. In comparison, when they only modeled for singular organisms (no chains) the resulting volume scattering strengths drastically underestimated their observed results. To produce appreciably high scattering strengths required impractically high sound speed contrasts,

ultimately suggesting that chain lengths need to be considered when modeling for accurate scattering strengths. *Kim et al.* (2010) concluded that the acoustic method may be a useful tool for detecting *C. polykrikoides* blooms in their initial stages, though indicated that further study is necessary.

In *Kim et al.* (2017) light-induced migration of a phytoplankton species was studied in the lab using a high-frequency ($40\,\mathrm{MHz}$) acoustic system. They assume simple spherical scattering physics, similar to the previous phytoplankton studies. Using just the acoustic system, they were able to measure migration speeds of the species but they conclude that independent measurements (e.g. by microscopy) of the speeds are needed to validate their accuracy.

Lastly, in the most recent article, *Kim et al.* (2018) developed an acoustic instrument capable of *in situ* measurements in the field and go through the performance evaluation of it both in the lab and following a field-deployment over three months to detect HABs (particularly, *Cochlodinium polykrikoides*), including efforts to differentiate species based on temporal variation. In their study, they do not rely on a scattering model to predict scattering levels but instead utilize a relative received level compared to a background reference. Their lab results showcased a positive correlation between concentration and scattering amplitude. However, the scattering amplitudes did not match to comparable concentrations found in the field – a result, they conclude, related to this phytoplankton's tendency to form longer chains (4 to 16 cells) in the open ocean compared to in the lab (1 to 2 cells). Despite the limitations, they conclude they were capable of providing both a precautionary level and a warning level for a HAB as it developed, increasing in concentration, over multiple weeks. Because they use relative amplitudes as a threshold no morphological study was able to be conducted.

## 1.3 Research Objectives

The acoustic methods presented above, particularly those concerning zooplankton and phytoplankton, provide the framework for my proposed research. Methods that have proven useful in the study of zooplankton (*Holliday et al.*, 1979; *Stanton et al.*, 1994, 2000; *Lavery et al.*, 2007) are thoroughly tested and can theoretically be applied to the study of phytoplankton as the initial work of *Blanc et al.* (2000) and *Kim et al.* (2010) have shown. This works improves previous phytoplankton studies by using a broadband acoustic system. The broadband treatment will allow for an in-depth spectral analysis of the backscatter including improved estimates of sound and density speed contrasts in addition to the possibility of categorizing species based on their characteristic spectra.

To this end, my research objectives are listed as follows:

1. Confirm that backscattering from phytoplankton is observable in the 0.5 - 10 MHz frequency range.
    - Develop a high-frequency broadband acoustic system that is capable of insonifying a lab-grown phytoplankton culture.
2. Determine if the selected species of phytoplankton can be resolved for a range of concentrations in the MHz frequency range. This includes:
    - Grow exemplar test species of phytoplankton to various concentrations
    - Use the system developed in (1) along with signal processing techniques and well-crafted waveforms to increase signal-to-noise ratios.
    - Demonstrate that the scattering strength varies with the independently measured biomass.
3. Describe the scatter of phytoplankton with different morphologies as a function of frequency. This includes:

- Determine if the species have distinguishable spectra.

4. Compare the backscatter results to theoretical models. This includes:

    - Use a statistical metric to identify the most appropriate model.
    - Fit (estimate) appropriate density ($g$) and sound speed ($h$) contrasts to each species.

5. Conclude if the method is appropriate for remote sensing subsurface blooms and to suggest possible improvements.

# CHAPTER 2

# SCATTERING PHYSICS & MODEL SPECIES

This chapter reviews the acoustic scattering theories that are relevant to small, weakly-scattering phytoplankton. The intention is to model the volume scattering strength from an ensemble of uniformly-distributed, discrete scatterers (the individual phytoplankters). Concepts such as the scattering amplitude will be defined and model equations presented.

## 2.1 Scattering Amplitudes

In order to measure the scattering from an ensemble of phytoplankton, we must first understand the acoustic response of a single phytoplankter target. The strength of the acoustic response depends significantly on the wavelength ($\lambda$) of the incident wave. In addition to wavelength, the response also depends on a number of physical parameters of the target, which together, I refer to as their *morphology*:

**Shape** The shape of a scatterer plays a large role such that it sets up the geometry of the system. Simple shapes (e.g. spheres, cylinders) lend themselves to symmetric solutions that allow for simple modal representations of the scattered pressure. When considering more complex shapes, analytic solutions may still be present if simplifications (e.g. if the object is weakly scattering) are made.

**Size** The size of a scatterer is defined by its corresponding shape dimensions. For spheres,

the size is determined by the radius ($a$). For prolate spheroids the semi-major ($a$) and semi-minor ($b$) axes are used. And for cylinders the length ($l$) and width ($w$) are used to define a length-to-width ratio.

**Composition** The composition of the scatterer is defined by the density ($g$) and sound speed ($h$) ratios

$$g = \rho_2/\rho_1, \qquad h = c_2/c_1 \tag{2.1}$$

where subscript '2' denotes a region bounded by the organism and '1' the water surrounding it. When shells are involved, (2.2.2), a third region must be defined to account for the new region. Together, $g$ and $h$, define the impedance contrast, affecting how the pressure wave reflects off and refracts through the scatterer.

When the acoustic wave interacts at all three levels of morphology, a scattering amplitude, $f$, can be defined that denotes what proportion of the incident wave reaches some point $\mathbf{r}$ in the system. Alternatively, this amplitude can be thought of as a scattering efficiency. In a sonar setup, the scattered pressure wave can be written in terms of the scattering amplitude as (*Stanton et al.*, 1998a)

$$P_{scatt} = P_{inc}\frac{e^{ikr}}{r}f \tag{2.2}$$

where $P_{inc}$ is the incident sound wave pressure, $i = \sqrt{-1}$, $k = 2\pi/\lambda$ is the incident wavenumber and $r$ is the distance between the receiever and scatterer in the far-field. The morphology of the object is embedded within the scattering amplitude, $f$. It is $f$ that is presented in the subsequent sections 2.2 and 2.3 for each unique model.

While $f$ is used throughout this section as the end product for the model equations, target strengths (TS) and volume scattering strengths ($S_v$) are more commonly plotted in the literature. Target strength in the backscattering direction relative to $1$ m$^2$ is expressed in terms of $f_{bs}$ as,

$$\mathrm{TS} = 10 \log_{10} |f_{bs}|^2 = 10 \log_{10} \sigma_{bs} \tag{2.3}$$

where the backscattering cross-section, $\sigma_{bs}$, is also introduced as an alternative definition. And, when considering an ensemble of scatterers, the volume scattering strength, $S_v$, becomes a more appropriate measure of the system. With an ensemble concentration of $N$ identical targets per unit volume, the volume scattering strength is related to TS as

$$S_v = \mathrm{TS} + 10 \log_{10} N \tag{2.4}$$

which can be seen simply as the summation of TS for each individual scatterer (and presented in log-space).

Furthermore, in the typical treatment of acoustic data, multiple pings in succession are analyzed together by averaging their scattering intensities and taking a mean ensemble concentration prior to logarithmic conversion,

$$\begin{aligned} \langle S_v \rangle &= \langle \mathrm{TS} \rangle + 10 \log_{10} \langle N \rangle \\ &= 10 \log_{10} \langle |f_{bs}|^2 \rangle + 10 \log_{10} \langle N \rangle \end{aligned} \tag{2.5}$$

*Stanton et al.* (1996, 1998a,b) discusses scattering from zooplankton as it relates to three major morphological groups: (1) fluid-like, (2) hard elastic shelled, and (3) gas-bearing. I have taken a similar approach by studying the scatter from morphologically distinct species of phytoplankton. A preliminary analysis of each species' morphology led me to define four possible primary scattering mechanisms: (1) fluid sphere, (2) fluid-filled spherical elastic shell, (3) DWBA fluid prolate sphere, and (4) DWBA fluid straight cylinder.

It should be noted that while the zooplankton studies (e.g. *Stanton et al.* (1998b); *Kristensen and Dalen* (1986)) are sometimes concerned with a preferred orientation of the

scatterer, I do not consider it for this study for any of the selected species of phytoplankton. Assuming a well-mixed water column and phytoplankton population, orientation is not expected to show any bias (and indeed may reduce the complexity of the problem to simple equivalent-sphere-like analysis). Additionally, nothing in the physiology or behaviour of the phytoplankton suggests a preferred orientation. Instead, all orientations are considered with equal probability and I am concerned only with the morphological features defined previously.

## 2.2 Exact Spherical Models

### 2.2.1 Fluid Sphere

A fluid sphere describes a spherical object containing a fluid with a different density and/or sound speed than the surrounding fluid. Incident acoustic waves can propagate into the sphere, but, being a fluid, the interior of the sphere cannot cannot support shear waves. The object is described by its radius, $a$, density, $\rho_2$, and sound speed, $c_2$. Surrounding the object is a fluid media with density, $\rho_1$, and sound speed, $c_1$.

With the sphere centered at the origin, the boundary conditions of the problem require the acoustic pressure, $P$, and the radial component of particle velocity, $u_r$, to be continuous across the boundary at $r = a$. The acoustic pressure must also satisfy the three-dimensional wave equation,

$$\nabla^2 P = (1/c^2)(\partial^2 P/\partial t^2)$$

The solution in spherical coordinates to this problem is shown by *Anderson* (1950) and results in a familiar spherical harmonic expression (equation 10 from *Anderson* (1950)),

$$P_{scatt} = P_{inc}\frac{i}{kr}e^{ikr}\sum_{m=0}^{\infty}(-1)^m\frac{2m+1}{1+iC_m}P_m(\cos\theta) \tag{2.6}$$

where $P_m$ are the Legendre polynomials as a function of the cosine of incident angle ($\theta$)

and $C_m$ consists of spherical Bessel functions and spherical Neumann functions (equation 9 from *Anderson* (1950)).

Comparing the above solution to equation 2.2, the scattering amplitude from a fluid sphere can be separated,

$$f_{\text{fl-sphere}} = \frac{i}{k} \sum_{m=0}^{\infty} (-1)^m \frac{2m+1}{1+iC_m} P_m(\cos\theta) \tag{2.7}$$

In Figure 2.1, the target strength (see equation 2.3) for equation 2.7 is plotted for an example fluid sphere with a diameter of 1 mm, $g = 1.043$, and $h = 1.053$. In the very-low $ka$ region ($ka \ll 1$) the scattering intensity is highly dependent on the frequency and size and increases at a rate proportional to $(ka)^4 a^2$. As $ka$ begins to approach 1 the curve tapers, reaching a maximum before decreasing. In the large $ka$ region ($ka > 1$) the minima and maxima showcase the constructive and destructive interference of the different $m$th-order partial scattered waves (e.g. waves diffracted around the circumference and those reflected of of the front interface.)

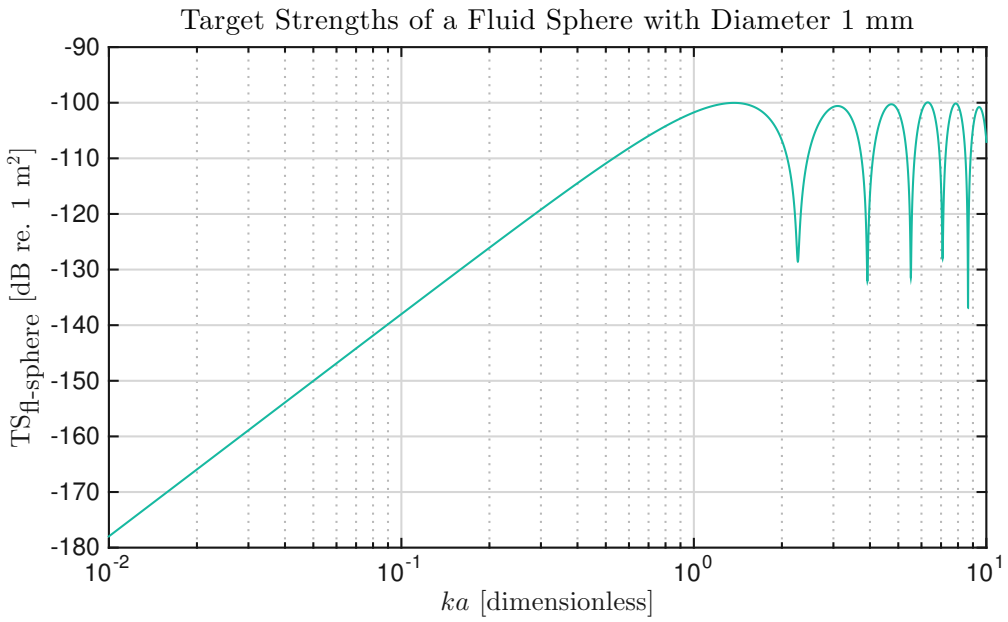


Figure 2.1: Predicted target strength versus $ka$ for a fluid sphere. Model parameters were defined as: diameter $= 1.0$ mm, g $= 1.043$, h $= 1.053$, sound speed (c) $= 1500$ m s$^{-1}$. Parameters were selected to be comparable to zooplankton characteristics found in literature.

Previous work has shown that applying the fluid sphere model to scattering from organisms does not require them to be composed entirely of liquid (*Blanc et al.*, 2000; *Stanton et al.*, 1998b). Rather, the fluid composition is an approximation of soft tissue where any shear waves are weak and quickly dampened. Generally, this means that the $g$ and $h$ of these tissues must be close to unity. The fluid that does exist such as the cytoplasm in a phytoplankter, will have $g$ and $h$ comparable to the tissue values. *Blanc et al.* (2000) went further in this approximation when analysing hard-shelled organisms by marginally increasing $g$ and $h$ to account for the increased effect of shell scatter. As stated before, further validation of this approximation is a goal of this thesis and in order to do so, an elastic shell model needs to be defined.

### 2.2.2 Fluid-Filled Spherical Elastic Shell

A fluid-filled spherical elastic shell describes a spherical object composed of three regions: (I) exterior fluid media with density, $\rho_1$, and sound speed, $c_1$, (II) an elastic shell of outer

radius $b$ and inner radius $a$, with density, $\rho_2$, compressional sound speed, $c_2$, and shear sound speed, $c_s$, and lastly (III) the interior fluid media with density, $\rho_3$, and sound speed, $c_3$. Density and sound speed contrasts are defined in comparison to the external media (e.g. $g_{21} = \rho_2/\rho_1$, $h_{31} = c_3/c_1$). For clarity, the regions and their parameters are presented as a schematic in Figure 2.2. Solving for the scattering amplitude for a spherical shell has a similar setup to that of the fluid sphere presented earlier. However, now the shell is capable of supporting shear waves and elasticity must be accounted for. A modal solution in terms of spherical harmonics is provided by *Gaunaurd and Werby* (1987),

$$f_{\text{shell}} = \frac{-i}{k} \sum_{m=0}^{\infty} (-1)^m (2m+1)[A_m P_m(\cos\theta)] \tag{2.8}$$

where $A_m$ is the ratio of two $(6 \times 6)$ determinants that satisfy combinations of displacement or stress boundary conditions at the surfaces of the shell dependent on shell thickness and its material (equation 3 in *Gaunaurd and Werby* (1987)).

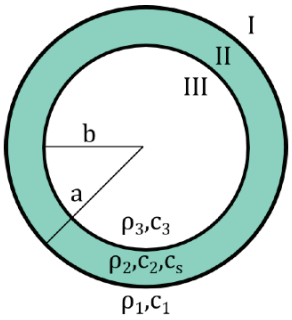


Figure 2.2: Geometric description of shelled scatterer. Region I is the surrounding fluid, region II is the shell and region III is the interior fluid. Density and sound speed parameters for each region are labelled.

In Figure 2.3 the fluid-filled spherical elastic shell model is shown for three different shell thicknesses and compared to the fluid-sphere model. It can be seen that both models (even for a larger thickness) behave similarly in low $ka$ where scattering intensity tends to increase as approximately $(ka)^4 a^2$. Intercomparing the shell model results, it can be seen that a thicker shell produces a much larger scattering response, in this case, of

approximately 30 dB. Indeed, it may be possible to compensate for this increased scattering by increasing the $g$ and $h$ parameters in a fluid model as suggested earlier. However, it can be seen that even in the low $ka$, a thin shell of a width 0.1% the radius can produce spiked returns where scatter amplitude can be lower than a comparable fluid sphere result. The differences between the models increases as $ka$ increases and by $ka = 0.5$ for a thickness of 2% (a reasonable value for phytoplankton shells) the *ad hoc* approach of increasing $g$ and $h$ to compensate between the models will no longer provide a reasonable estimate. This suggests that for sonar systems with a reasonably high operational $ka$ (high-frequency and/or large organism size) the model used in analysis may have a profound impact on interpretation of scattering results.

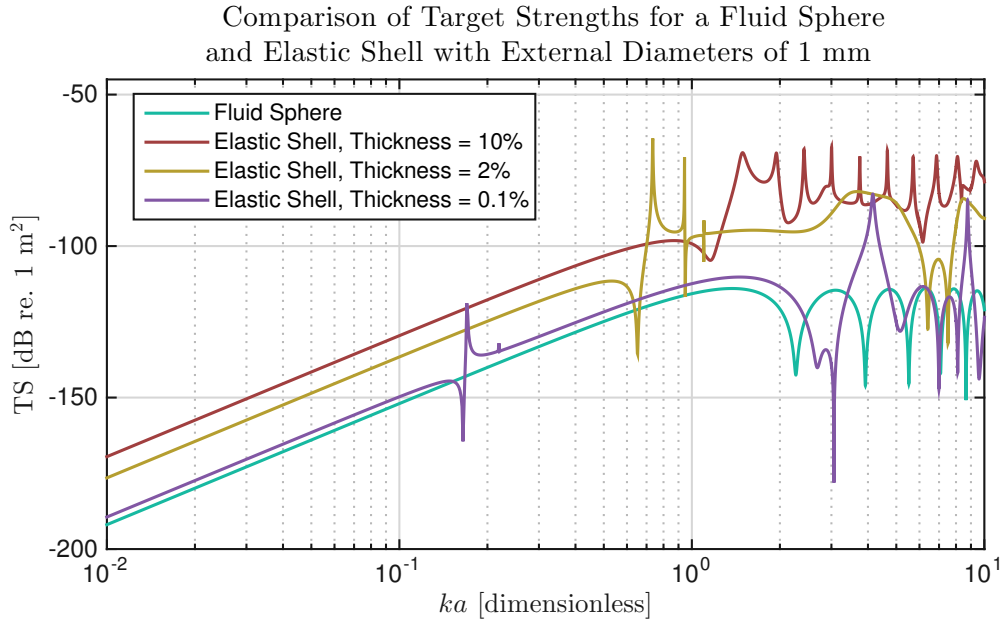


Figure 2.3: Predicted target strength versus $ka$ for a fluid sphere and elastic shells of two thicknesses. The fluid sphere was parameterized with a diameter $d = 1.0$ mm, $g = 1.030$, $h = 1.009$, and $c = 1500$ m s$^{-1}$. The shell models were paramaterized with outer radii $b = 1.0$ mm, inner radii $a_{10\%} = 0.1$ mm, $a_{2\%} = 0.02$ mm and $a_{0.1\%} = 0.001$ mm, $g_{21} = 2.520$, $g_{31} = 1.030$, $h_{21} = 1.053$, $h_{31} = 1.009$, $c_s = 1579.500$ m s$^{-1}$. Parameters were selected to match those presented in *Blanc et al.* (2000)

## 2.3 DWBA Scattering Models

For geometries more complex than spheres, solutions no longer take a modal form. In this case, an alternative solution relying on the Born approximation (BA) may be derived. The principle concept of the BA is to approximate the scattered pressure inside a scattering volume as the unperturbed, incident pressure field. This approximation is valid for cases where the scattered wave is much smaller than the incident wave (*Morse and Ingard*, 1968). In the case of scattering from phytoplankton (and similarly in zooplankton), the organisms can be considered to be *weakly scattering bodies* and so the approximation holds.

The basic form of the BA solution is of a volume integration of the pressure field and material properties bounded by the scatterer's arbitrary geometry. The distorted-waved Born approximation (DWBA) improves the accuracy of the BA by including first-order weak interactions on the pressure field within the scattering volume. To do this, the incident wavenumbers (in the integration) are replaced with the wavenumber vector of the internal medium. *Morse and Ingard* (1968) derives the distorted-wave Born approximation (DWBA) backscattering as a general volume integral over a finite size body as

$$f_{\text{bs-dwba}} = \frac{k_1^2}{4\pi} \iiint_{\text{v}} (\gamma_\kappa - \gamma_\rho) e^{2i\mathbf{k}_{2i}\cdot\mathbf{r}_\text{v}} \text{dV} \tag{2.9}$$

where $k_1$ is the incident wavenumber, the material properties of the scatterer are expressed in terms of compressibility ($\kappa$, where $\kappa_i = (\rho_i c_i^2)^{-1}$) and density ($\rho$) as,

$$\gamma_\kappa = \frac{\kappa_2 - \kappa_1}{\kappa_1} = \frac{1 - gh^2}{gh^2} \tag{2.10}$$

$$\gamma_\rho = \frac{\rho_2 - \rho_1}{\rho_2} = \frac{g - 1}{g} \tag{2.11}$$

and where $\mathbf{k}_{2i}$ is the wavenumber vector of the incident sound evaluated in the interior of volume, $V$, and $\mathbf{r}_v$ is the position vector of any volume element. In all cases, the

subscript "1" indicates parameters of the surrounding medium and the subscript "2" indicates parameters within the scattering volume.

Ultimately, the DWBA formulation is valid for all orientations, shapes and frequencies provided that the objects are weakly scattering. However, two relatively simple geometries that I will consider in this study of phytoplankton are the prolate sphere and the straight-finite cylinder.

Geometrically speaking, both the prolate sphere and straight-finite cylinder can be similarly broken down into a coaxial stack of infinitesimally thin circles. With this geometric symmetry and by further assuming a radially homogeneous interior, the volume integration in equation 2.9 can be solved analytically for two dimensions and the formulation is reduced to a line integral along the length of the scattering volume (*Stanton et al.*, 1998b),

$$f_{\text{bs-dwba}} = \frac{k_1}{4} \int_{\mathbf{r}_{\text{pos}}} a(\gamma_k - \gamma_\rho) e^{2i\mathbf{k}_{2i}\cdot\mathbf{r}_{\text{pos}}} \frac{J_1(2k_2 a\cos(\beta_{tilt}))}{\cos(\beta_{tilt})} \mathrm{d}\mathbf{r}_{pos} \tag{2.12}$$

where $\mathbf{r}_{\text{pos}}$ is the position vector of the axis of the cylinder, $a$ is the radius of any given circular cross-section, $J_1$ is the Bessel function of the first kind, and $\beta_{tilt}$ is the tilt angle of any infinitesimally thin cross-section at an arbitrary point $\mathbf{r}_{\text{pos}}$ relative to $\mathbf{k}_i$. This model can be parameterized with any arbitrary curve and material properties that can vary along the length.

For my purposes, I assume that the material properties are homogeneous throughout and the scattering volumes are to be prolate spheroids or cylinders defined by $a$ and a length, $L$, embedded in the integration limits.

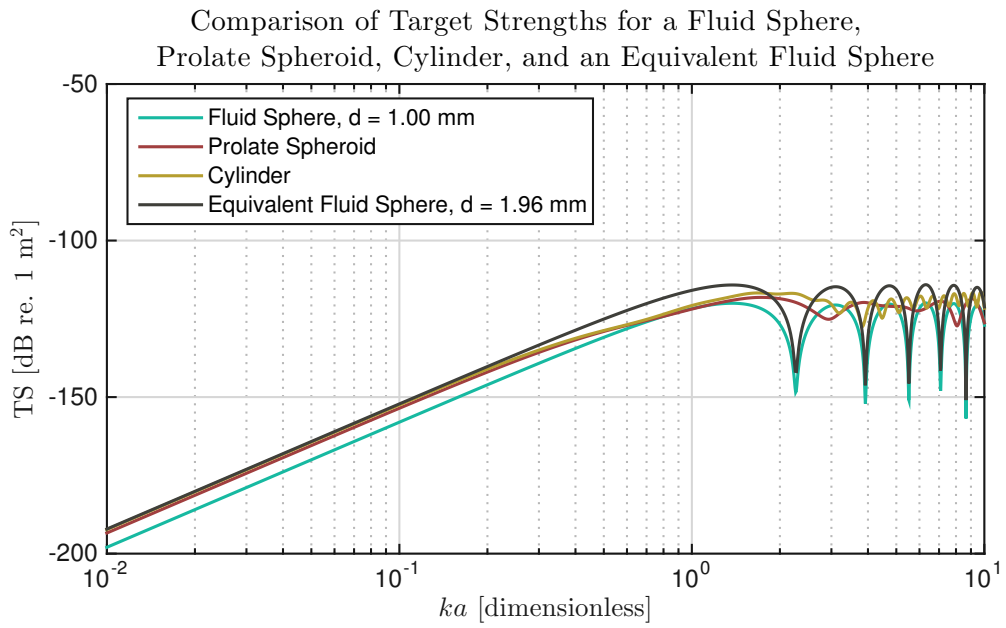


Figure 2.4: Target strength versus $ka$ for a fluid sphere, prolate sphere, cylinder and an equivalent fluid sphere. All models share the parameters $g = 1.030$, $h = 1.009$, and $c = 1500$ m s$^{-1}$. The fluid sphere has a diameter $d = 1.0$ mm. Both the prolate sphere and cylinder have a width of $w = 1.0$ mm and have length-to-width ratios of 5. The TS for the prolate spheroid and cylinder is calculated by averaging over a distribution of orientations relative to the acoustic source. The equivalent fluid sphere was calculated for the cylinder, resulting in a diameter, $d = 1.96$ mm.

In Figure 2.4 the models are shown for dimensionally similar objects in order to showcase the differences the shape has in their scattering properties. The same fluid sphere with $d = 1.00$ mm from the two previous backscatter figures is shown as a reference. Both the minor-axis width of the prolate sphere and the diameter of the cylinder are equal to 1.00 mm and length-to-width ratios of 5 (i.e. lengths equal to 5.00 mm). The differences between prolate spheres and cylinders for $ka < 1$ are small with the cylinder having an additional 2 dB intensity with this particular length-to-width ratio. This difference would decrease as the length-to-width ratio tended to 1. As $ka$ increases toward 1, the intensity difference narrows to a point where the two models are approximately equivalent. Once $ka > 1$ the two models diverge more dramatically with varying oscillatory behaviour. The other comparison made in Figure 2.4 is the one between a cylinder and its equivalent fluid-sphere. As one expects, the two models are very similar at low $ka$ with intensity differences

less than 0.2 dB. However, the two models begin to diverge at around $ka = 0.25$ when the cylinder begins to taper off more quickly than the equivalent fluid-sphere resulting in an intensity difference up to 7 dB before the fluid-sphere amplitude begins falling off into its first null.

## 2.4 Exemplar Phytoplankton Test Species

Achieving varied morphologies was the primary motivation when selecting the phytoplankton species to study. However, I was limited to a subset of approximately 100 species that were immediately available and familiar to Dr. Hugh MacIntyre's lab – the group I relied on for successful growth and maintenance of the cultures. From this subset I identified five exemplar species that showcased a range of morphologies and whose sizes were relatively large to achieve the highest possible $S_v$.

Of those five, four were successfully grown and insonified in this study: (1) *Alexandrium andersonii*, (2) *Eutreptiella gymnastica*, (3) *Ditylum brightwellii*, and (4) *Stephanopyxis palmeriana*. The fifth species *Coscinodiscus wailesii* proved too difficult to grow to a sufficient density. These cultures were obtained from the National Center for Marine Algae and Microbiota (Boothbay, ME, USA). The strain designations are given below as are brief summaries of their ecology, morphology and the motivation for choosing them for this study.

### 2.4.1 *Alexandrium andersonii* (CCMP3376)

*Alexandrium andersonii* (Figure 2.5a) is a potentially-toxic dinoflagellate that contributes to harmful algal blooms and paralytic shellfish poisoning. They are found primarily in coastal regions and have been the focus of numerous studies due to their potential impact on human and other biological life (*Anderson et al.*, 2012). *A. andersonii* is an armoured dinoflagellate that has a series of rigid overlapping cellulose plates creating its theca. A small, ridged depression forms its girdle approximately around the circumference. It is

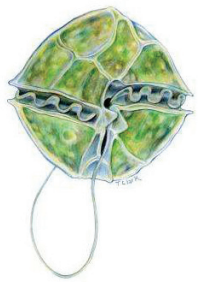

(a) *A. fundyense*

(b) *D. brightwellii*

(c) *E. gymnastica*

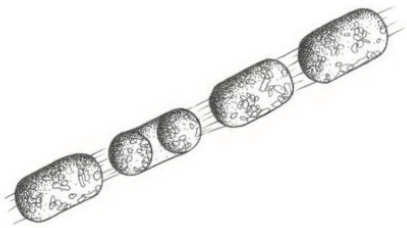

(d) *S. palmeriana*

Figure 2.5: Illustrations of the exemplar test species and their morphologies. (a) Drawing of *A. fundyense*, a morphologically similar species to *A. andersonii*. The thecal plates can be seen in both hemispheres of the organism, separated by the girdle. Image from *EOL - Encyclopedia of Life*. (b) Drawing of *D. brightwellii*. The prominent, acoustically transparent spines are seen at the poles. Dark, shaded, vacuoles are seen in the interior of the cylindrical silicous shell. Image from *Smithsonian Institute*. (c) Drawing of *E. gymnastica* in a relatively uniform rest-state, taking the shape of a prolate spheroid. Surrounding the cell-wall is some organic matter that is not present on the majority of the organisms. Image adapted from *Throndsen* (1969). (d) Drawing of *S. palmeriana*. Shown is a chain comprised of 4 individual organisms connected by thin spines. Thin, silicious cell walls surround each organism. Image from *USCS Ocean Data Center*.

approximately spherical in shape and has been reported to have a diameter of roughly $40\,\mu\mathrm{m}$.

This species was selected primarily for its spherical shape and its relatively large size; spherical morphologies usually being restricted to smaller species. The thecal plates also provide an opportunity to compare the spherical shell and fluid sphere models and determine whether the material properties of the cellulose composition influence the scatter significantly.

### 2.4.2 *Ditylum brightwellii* (CCMP358)

*Ditylum brightwellii* (Figure 2.5b) is an example of a centric diatom. It is found in all global oceans except in polar waters (*Round et al.*, 1990). Characteristic of diatoms, it is surrounded by a silicious cell wall forming the frustule. Average lengths of the organisms are reported to be between 30-250 $\mu$m and 3-9 times the diameter. The cross-sectional shape is primarily triangular with rounded corners, which, at the scales the acoustic system is sensitive to can be approximated as circular. Each cell has thin hollow tubes extending from their poles that are so thin as to be acoustically transparent at the wavelengths explored in this study. Other small irregularities in their shape (e.g. girdle, pores) should not affect the scatter. The cells are often solitary but short (2-3 unit) chains may infrequently form in rapidly growing populations (*Round et al.*, 1990). Due to their rare occurrence, the chains are not expected to have a significant effect on the total $S_v$.

This species was selected for its characteristic frustule. The silicious material has estimated material properties of $g = 2.15$, $h = 3.93$ compared to seawater and $c_s = 3700\ \mathrm{m\ s^{-1}}$ (*Lide*, 2005), suggesting a possible strong influence on the overall scattering amplitude of the organism. The models tested for this this organism include the the fluid-sphere, the DWBA straight cylinder, and the elastic spherical shell.

### 2.4.3 *Eutreptiella gymnastica* (CCMP1594)

*Eutreptiella gymnastica* (Figure 2.5c) is an example of a euglanoid found primarily in Norwegian coastal waters (*Throndsen*, 1969). The cellular boundary is soft and highly deformable but a 'rest state' of the cell takes the shape of a prolate spheroid. In this rest state, or average state, the lengths have been reported to be 10-60 $\mu$m and 3-5 times the diameter.

A unique property of the euglenophytes is their movement. While they can use flagella, they can alternatively move by metaboly, a rhythmic undulation of their shape to propel them forward. During this kind of movement, the cell expands and contracts along

a single axis thereby increasing and decreasing its length-to-width ratio. This is not a rapid process relative to acoustic transmission speeds and is observed to occur on an individual basis (i.e. the culture does not deform uniformly.)

This species is the exemplar candidate for the DWBA prolate spheroid model. However, because of its mobility and small size, a fluid sphere may also be a good approximation.

### 2.4.4 *Stephanopyxis palmeriana* (CCMP814)

*Stephanopyxis palmeriana* (Figure 2.5d) is another example of a centric diatom. It is found globally in temperate and subtropical regions (*Cupp*, 1943). In contrast to *D. brightwellii*, this species is chain-forming with chain lengths ranging from 2 to 16 units. A silicious cell wall surrounds each cell and is not present between the chain connections (*Cupp*, 1943). The individual cells have been reported to be 30-35 $\mu$m in length and 0.75-1.25 times the diameter. Their shape is cylindrical and capped with hemispheres on each end. The chains form with the cells arranged end-to-end with minimal spacing, remaining straight as the chain length increases. Because of the minimal gap between cells, it is expected that bulk scattering will be from the chain as a whole, and not from the individual cells.

This species was selected to analyze the scatter from a chain-forming species. The chain's effect on scatter can be determined by contrasting model results of the fluid sphere and the DWBA straight cylinder; and the shell's influence can be determined by studying the elastic spherical shell in comparison to the fluid sphere model.

# CHAPTER 3

# DATA ACQUISITION AND PROCESSING

To observe and compare the scattering spectra of different phytoplankton species to theory, two types of data were collected: acoustical and biological. The acoustic data were collected with a sonar system that was developed based on a previous design by *Lavery and Ross* (2007). The collection of biological data were collected using multiple fluorometers, a flow cytometer and a microscope provided by Dr. MacIntyre's lab. The biological data had two objectives, (1) monitor the health of the culture's growth prior to insonification and (2) provide independent measures of size and abundance to assist in the interpretation of the acoustic data set.

In this chapter I detail the methods and instruments used to collect both the acoustic and biological data as well as the data processing steps used when analyzing the acoustical and biological data.

## 3.1 Acoustical Data Collection

The sonar system that collected the acoustical data consists of a bi-static arrangement of three pairs of broadband transducers that in total cover an operational frequency range of 0.75 to $6.90\,\mathrm{MHz}$. A linear, frequency-modulated signal (chirp; or sweep) was used to cover the transducer bandwidths (see Table 3.1). The transmission and reception of signals were controlled by a custom LabView program interfacing with PCI cards that functioned

as a waveform generator for transmitting and a digitizer for receiving the acoustic signal.

Both the transmit and receive signals were amplified to compensate for the expected weak scattering. The transmit signal underwent $50\,\mathrm{dB}$ of gain (ENI 240L). The received signal was sent through a pair of amplifiers. First, it was amplified by $34\,\mathrm{dB}$ (Panametrics NDT Preamp). Second, it was amplified by $50\,\mathrm{dB}$ (Krohn-Hite 3940) when using $1.0\,\mathrm{MHz}$ transducers and $40\,\mathrm{dB}$ when using 2.25 and $5.0\,\mathrm{MHz}$ transducers. Different amplification levels were used to maximize the received signal between -6 and $6\,\mathrm{V}$, the voltage limits of the digitizer, thereby exploiting the full dynamic range of the digitizer.

### 3.1.1 Bi-static Transducer Array

The transducers were mounted in the apparatus shown in Figure 3.1. It was designed to hold two pairs of transducers to maximize experimental efficiency while limiting its dimensional footprint. The transducers were vibrationally isolated from the apparatus by rubber gaskets seated in plastic blocks. The gaskets provide a strong friction-fit for the transducers and were further reinforced by a small set screw. The plastic blocks each housed one transducer from each pair. The blocks can be freely rotated and locked into place. Rotating the blocks changes the focal distance and separation angle of the transducer pair. Over the course of the experiments, the angle was set to $25^\circ$. This angle gave a focus approximately $15\,\mathrm{cm}$ away – a distance which, after time-gating, does not extend past the bottom boundary. A threaded rod that allowed for vertical control connected the plastic blocks to braces that were secured to the top of the experimental tanks. For the duration of the experiments, the angle of the blocks was not altered to ensure consistency between experiments and calibration.

The broadband transducers used were manufactured by Olympus-NDT, formerly NDT-Panametrics. Transducer specifications and their operational frequencies are shown in Table 3.1. The pair of National Instruments PCI cards (NI 5412 and NI 5122) that handled the transmitting and receiving were both capable of a $100\,\mathrm{MHz}$ sampling rate, surpassing the necessary Nyquist frequencies.

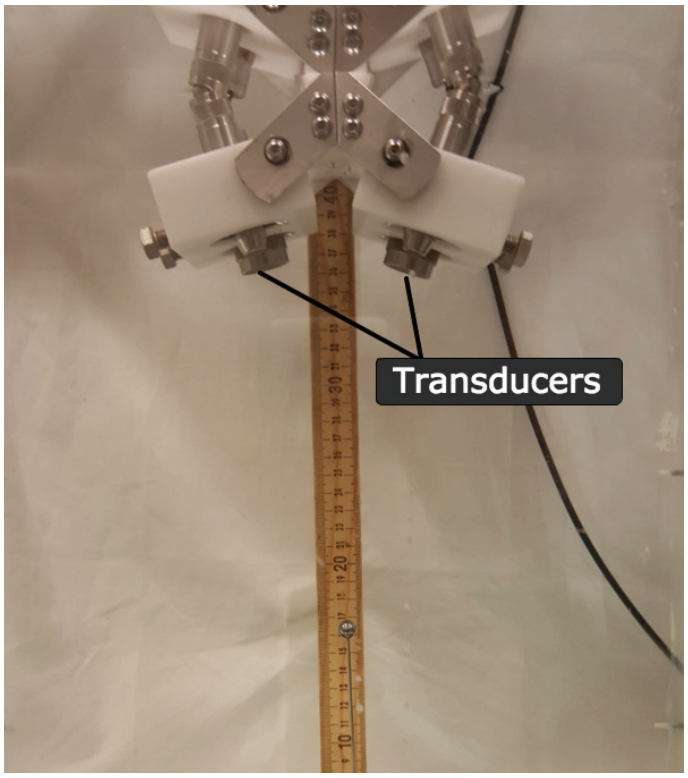


Figure 3.1: The acoustic apparatus design for this experiment. As pictured, it is set up for acoustic system calibration. The transducers are labelled. The blocks (of white plastic) encased the transducers. At the top of the image, the apparatus is reflected at the water's surface.

### 3.1.2 Test Tanks

A set of at least 4 identical test tanks were needed for the experiments. The tanks needed to be wide enough to accommodate the transducer array and to eliminate possible sidewall reflections from the widening beam patterns, and deep enough so that the insonification volume was in the far field, or at least past the last pressure maximum (see Table 3.1 for calculated distances.) However, the tanks could not be so large that the culture growth time was inefficient. It was determined that the effect of sidewall reflections is negligible when the tank diameter exceeds the array width, putting a lower bound on possible tank diameters of approximately 20 cm. The depth was restricted by the $2.25\,\mathrm{MHz}$ transducers whose last critical maximum was calculated to be $13.42\,\mathrm{cm}$, putting a lower bound on tank depths of $15\,\mathrm{cm}$ (to allow for at least a $2\,\mathrm{cm}$ insonification volume length). Lastly, the tank would

Table 3.1: Transducers used during the experiments and their element diameters. The Part Numbers are their designation by the manufacturer, Olympus-NDT. $R_{c,centre}$, denotes the critical distance, or last pressure maximum, for a circular piston transducer. It was calculated as $R_c = a^2/\lambda_{centre}$ (***Medwin and Clay***, 1998) where $a$ is the transducer radius and $\lambda_{centre}$ is its centre wavelength (calculated from the frequency using a water soundspeed of $1520\,\mathrm{m\,s^{-1}}$.) Note that while the 10 MHz transducer was used during the tests, its results are not analyzed due to very poor signal-to-noise caused by instrument limitations.

| **Frequency (MHz)** | | | **Transducer Part No.** | **Element Diameter (mm)** | $R_{c.centre}$ **(cm)** |
|---|---|---|---|---|---|
| *Min* | *Center* | *Max* | | | |
| 0.75 | 1.00 | 1.30 | V302-SU | 25.40 | 10.61 |
| 1.25 | 2.25 | 3.25 | V305-SU | 19.05 | 13.42 |
| 2.60 | 5.00 | 6.90 | V310-SU | 6.35 | 3.32 |
| 6.10 | 10.00 | 12.50 | V312-SU | 6.35 | 6.63 |

ideally be cylindrical to assist with symmetry. Beyond their dimensions, the tanks needed to meet requirements for use in growing phytoplankton mono-cultures. Most importantly, they needed to be sufficiently translucent to allow passage of high light levels; autoclavable; and air tight to limit the risk of contamination during their long growth periods. To fulfill these requirements, $20\,\mathrm{L}$ Nalgene™ Polycarbonate Carboys (ThermoFisher Scientific cat. no. 2251-0050PK) were selected. These carboys were sufficiently large, cylindrical, optically transparent, and autoclavable at both high temperature and pressure.

The carboy opening was initially too small to allow the acoustic array access. Thus, the top portion of the carboy, just past the neck's widening, was removed. The removed piece was inverted and used to make a friction-sealed lid. The friction-seal, secured further with tape, was judged to be sufficiently air-tight to limit contamination during culture growth.

The tanks were further modified with a glass and rubber spigot, sealed with an adjustable clamp on both the vessel's side and lid. The side access allowed for sample

collection used for monitoring the culture's growth and physiological status while the lid's access was used for adding a sodium bicarbonate solutions at regular intervals during growth (to prevent carbon limitation). These spigots limited the risk of air contamination by not having to remove the lid for basic maintenance. The final tank design is shown in Figure 3.2.

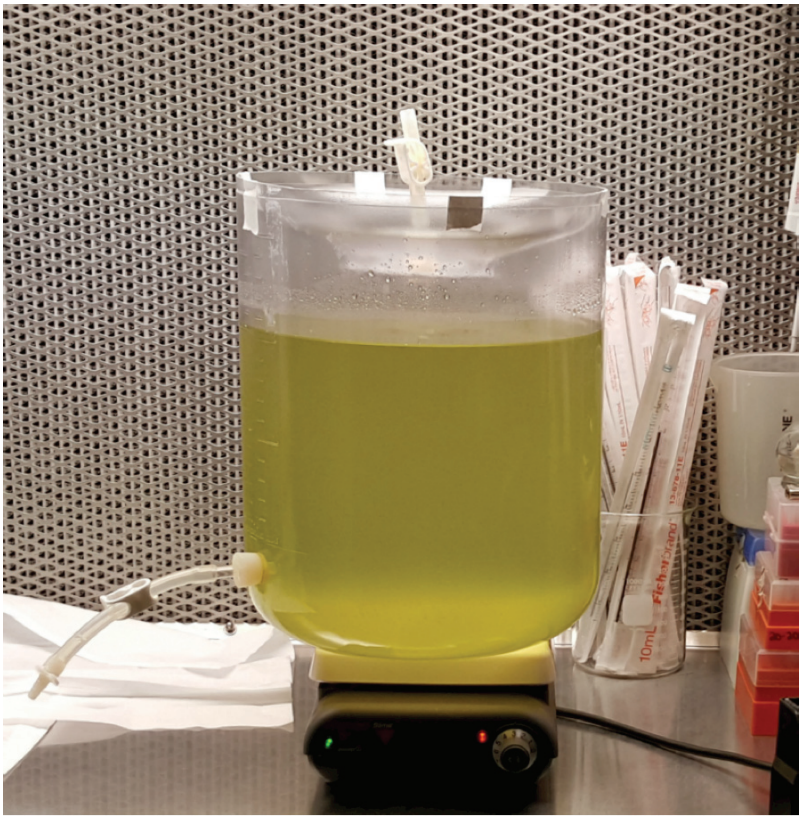

Figure 3.2: The 20 L test tank photographed just prior to taking acoustic measurements of *E. gymnastica*. Volume of culture was limited to 15 L. The spigot can be seen on the left side of the tank. The tube opening at the top was used to inject the sodium bicarbonate solution.

### 3.1.3 Labview Sonar Software

Software was developed in LabView to control the transmitting, receiving and data logging of the sonar system. The program was comprised of three virtual instruments, or VIs, each responsible for one of the aforementioned control tasks. Each VI introduced constants and user-defined variables and then issued them to the appropriate PCI card.

The transmission VI interfaced with the NI 5412 PCI waveform generator to control the transmit pulse. This VI allows the user to select between a sine wave or chirp signal and subsequently the signal length (ms), sample rate (Hz), ping delay (sec) and number of pings (integer). For sine-wave signals, amplitude (V) and frequency (MHz) are user defined. For a chirp signal, the beginning and end frequency are user-defined as well as the amplitude. Only chirp signals were used in this experiment.

The receiving VI controlled the NI 5122 PCI digitizer and connected to the receiving transducer. The user defined a sample rate (Hz) and record length (ms). The software confirms that the record length exceeds the pulse length. In this VI, the digitizer's clock is synchronized to the waveform generator's. The clock synchronization ensures that the digitizer begins recording precisely when the waveform generator starts its transmission.

Data acquired by the digitizer were saved via the third VI. It is capable of handling up to two input signals. During these experiments, the transmit and receive signal were both recorded. The transmit signal was later used during pulse compression (see Section 3.3.1. The signal amplitudes and time were collected as two data columns for each ping. The number of rows depends on the record length and sample rate set by the user. Subsequent pings were concatenated onto the first until all transmissions were completed. The matrix containing all the pings was then saved as a binary file. Alongside the data file, a log file was generated that details all the settings used in transmission and receiving and any additional user-entered comments.

## 3.2 Biological Data Collection

The biological observations were done using equipment provided by Dr. MacIntyre's lab. Three different fluorometers were used alongside a flow cytometer.

When monitoring the growth of the organisms, all instruments were used in conjunction to determine the health of the culture and to determine a biomass and concentration.

### 3.2.1 Cultivation of Phytoplankton Cultures

Culture growth began with an innoculation of each species from a stock culture that is maintained by the MacIntyre group. The first innoculation was done in a 250-mL sealed vessel and as the culture density increased, it was transferred into larger vessels until it could be added with sufficient density to the test tanks with a final volume of $15\,\mathrm{L}$. All smaller vessels used in culturing were cleaned prior to use by soaking in a 5% Micro-90 cleaning solution (Z281506, Sigma Aldrich) and then in a 2% HCl bath, rinsing with E-pure water (Barnstead Nanopure/APS Water Services Corporation, Lake Balboa, CA, USA) after each cleaning step. The largest (and final) test-tanks used were only submerged in the 2% HCl bath and rinsed with E-pure water. Each vessel was sterilized in an autoclave at $121\,^{\circ}\mathrm{C}$ and $15\,\mathrm{psi}$ prior to being used and during transfer. The density sufficient for transfer was determined by following the steps in Sections 3.2.2 and 3.2.3 on a daily to every-three-day schedule. Transferring of cultures was done by Shannah Rastin in the MacIntyre lab inside a sterile laminar-flow hood to minimize risk of contamination. The flow hood has a constant positive air pressure preventing ambient room air from entering the hood (in contrast to a fume hood that is held at a negative pressure, preventing air from leaving).

The culture vessels were kept inside incubators over the entire growth period. A light:dark cycle of 12:12h was applied to regulate the growth. Temperature was held between $22^{\circ}$C and $26^{\circ}$C over the duration of all the experiments.

In order to keep the cultures well mixed (to prevent settling and to provide even light levels) I inverted the vessels every day or every second day. Inversion was not possible in the final test tanks so a stir bar was added and the vessels placed on a stir plate inside the incubators. The stir speed was set so that no visible settling occurred. I note that there was some settling on and around the spigot's plastic stopper (see the slight discolouration on the side spigot in Figure 3.2) due to decreasing water velocity but this had no lasting impact on the overall growth or maintenance.

Each subsequent dilution was done with an enriched growth medium: L1 (*Guillard and Hargraves*, 1993) for *A. andersonii* and *E. gymnastica*; and f/2 (*Guillard*, 1975) for *D. brightwellii* and *S. palmeriana* that contain the necessary micro and macro nutrients for growth. To prevent carbon limitation on growth, $\sim 10\,\mathrm{mL}$ of sodium bicarbonate solution (10 molar concentration) was injected once every two to four days. This was equivalent to an addition of 7 mmol/L, well above the saturated concentration of 2 mmol/L. Excess $CO_2$ would be lost through atmospheric equilibration. The volume change from this added media is insignificant and not accounted for (i.e. $15\,\mathrm{L}$ was used when calculating dilution values).

### 3.2.2 Extracting Samples from the Phytoplankton Culture: Protocol

The sampling procedure follows instruction and procedure commonly used in the MacIntyre lab (*MacIntyre et al.*, 2018). For each physical sample extracted from the phytoplankton culture, the following steps were followed:

1. A $10\,\mathrm{mL}$ sample is taken from the well mixed culture using sterile pipettes or the spigot on the side of the largest vessel and placed in a vial cleaned with the 2% HCl and E-pure water rinse procedure described above.

2. After dark-acclimation for 20 minutes to allow fluorescence quenching to relax, variable chlorophyll fluorescence was measured in a *Fluorescence Induction and Relaxation* (FIRe) (*Brand et al.*, 1981; *Guillard*, 1973) fluorometer (Satlantic, Halifax, NS) to estimate the quantum yield of PSII electron transport, Fv/Fm, a parameter routinely used to assess imposition of stress, and the minimum fluorescence, F0, for estimating growth rate (*Brand et al.*, 1981). The fluorometer was blanked with and standardized with a 100-M solution of Rhodamine b. For a full description, see *MacIntyre et al.* (2018).

3. $1\,\mathrm{mL}$ of the sample is pipetted into a small cuvette for flow cytometric analysis.

Three replicates of $300\,\mu L$ each are run through the flow cytometer (BD Accuri™ C6) to obtain cell abundance counts.

4. $200\,\mu L$ of the sample is pipetted into a vial containing 6 mL of a 3:2 V:V mixture of 90% acetone and dimethyl sulfoxide (*Shoaf and Lium*, 1976) to extract pigments for fluorometric determination of chlorophyll *a* (*Welschmeyer*, 1994) using a Turner 10AU fluorometer (Turner Designs, Sunnyvale, CA, USA.) The fluorometer is blanked with acetone:DMSO and calibrated with purified chlorophyll *a* (Z281506, Sigma Aldritch).

5. The remaining (approximately) $8\,mL$ of sample is inverted to ensure it is well mixed and a small volume is extracted to prepare multiple slides for microscopic analysis (AX10 microscope with an AxioCam ERc5s camera; Zeiss, Germany.)

### 3.2.3 Tracking Health and Abundance

To track the growth and physiological status of the culture, the sampling procedure detailed above was completed every one to three days. An exponential growth phase is expected for a healthy culture followed by a plateau of slowing growth as it exhausts the nutrients required to sustain growth. During the course of the experiments, the exponential growth phase lasted between 2 weeks and 5 weeks. Only once did a culture fail to reach a stationary phase and in this case a second innoculation was able to reach it without issue. Once the cultures were at a maximum concentration in the acoustic test tanks, the acoustic measurements were conducted within the following days.

Measuring the abundance (or concentration) of the cultures was done using flow cytometry (i.e. Step 3 of Section 3.2.2). *S. palmeriana* abundance could not be determined with cytometric methods and was instead determined by manual counting using samples collected on a haemocytometer, as discussed at the end of this section. Cytometry data files were created and analysed in the BD Accuri™ software. The cytometer counted bacteria and any other organisms in the sample alongside the phytoplankton. Cell counts

were corrected for the bacteria and non-living particulate material (e.g. precipitates in the growth medium) by gating the data based on chlorophyll *a* fluorescence and forward-angle light scatter, a proxy for cell size. Bacterial cells are at least an order of magnitude smaller than the phytoplankton species used in these experiments. However, that does not mean that there was no contamination from other species of phytoplankton in the desired mono-culture. Sources of the contamination may have come from improper handling in the flow hood or even intrusion from aerosolized species due to non air-tight lids.

To verify that the phytoplankton cultures contained a single taxon, the cluster attributed to the phytoplankton based on chlorophyll *a* fluorescence and forward scatter was also tested for any bi-variance by comparing these same properties on different wavelengths filtered in the cytometer. Ultimately, the cultures were found to be free from any detectable contamination with the cytometer and further confirmed by the microscopic analysis of the samples where no other organisms were seen.

Getting an accurate estimate of concentration of *S. palmeriana* proved difficult due to its long chain lengths. Some initial samples were analysed by cytometry but they clogged the flow through the instrument, preventing accurate count measurements. Thus, concentrations were measured manually with a haemocytometer.

A haemocytometer is a microscopic slide with a precise grid etched onto the surface. Assuming a uniform thickness of sample between the cover slide and haemocytometer, a concentration can be determined by counting the individual organisms per grid unit. While the accuracy of this method is not as high as the flow cytometer, it allowed for an estimate of concentration to be made.

### 3.2.4 Size Distribution

The size distributions of the phytoplankton populations were determined by analyzing micrographs (images taken with a microscope). An example micrograph of each species is shown in Figure 3.3. During growth of the cultures, multiple slides were prepared each time the culture was sampled. For each of these slides, individual organisms were isolated

and micrographs taken. During the acoustic measurements, multiple slides were prepared at each dilution (details in Section 3.3) and later combined to represent the size distribution of the total population.

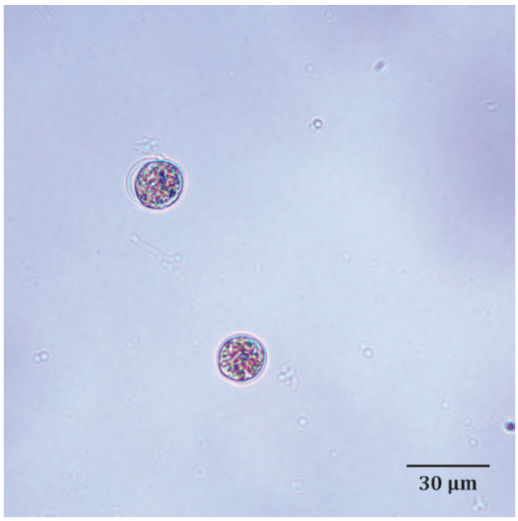


(a) *Alexandrium andersonii*

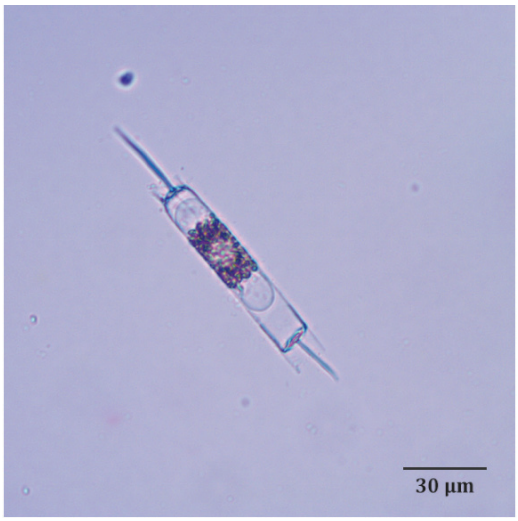


(b) *Ditylum brightwellii*

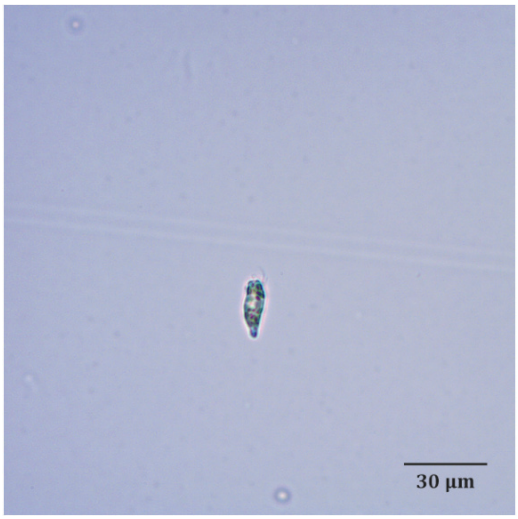


(c) *Eutreptiella gymnastica*

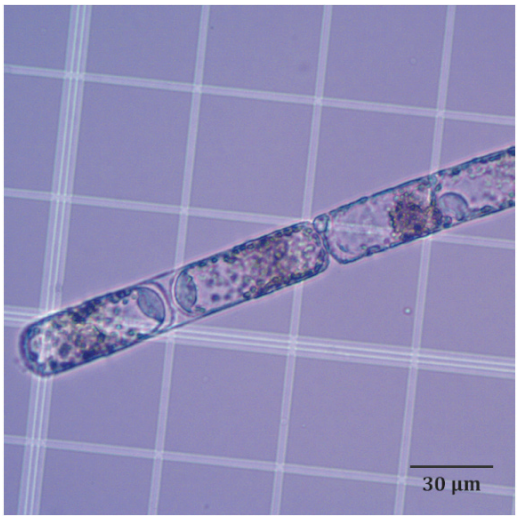


(d) *Stephanopyxis palmeriana*

Figure 3.3: Micrographs of the studied species. Scale bars are seen in the lower right corner. The range of morphologies are clearly seen. (a) *A. andersonii*. (b) *D. brightwellii*. (c) *E. gymnastica*. (d) *S. palmeriana*.

Organism lengths and widths were extracted manually from micrograph images using the measurement tool in the image processing software imageJ. For *A. andersonii*,

only the radii were recorded. For *D. brightwellii*, *E. gymnastica* and *S. palmeriana* the major and minor axes were recorded. In the case of *S. palmeriana* the individual cell units were measured and averaged for each chain and the organism's corresponding number of cells per chain (i.e. chain length) were recorded.

However, upon reviewing the determined sizes and comparing them to past culture measurements by the MacIntyre Lab and in subsequent publications (*MacIntyre and Cullen*, 2016; *MacIntyre et al.*, 2018), it was determined that these measurements were likely incorrect by an unaccounted for scaling parameter. It was assumed that this was likely due to an incorrect calibration (either old or improper) in the microscopic camera used for imaging.

To correct for this calibration error, images of *S. palmeriana* that were taken on an Improved Neubauer haemocytometer (schematic in Figure 3.4) were remeasured. In particular, the observed grid-spacing of the haemocytometer were correlated to its known dimensions and a corrected scaling factor ($\mu = L_{\text{actual}}/L_{\text{observed}}$, where $L$ denotes a length) was calculated. A total of forty separate measurements of the grids were extracted. The mean scaling factor was calculated to be $\mu = 2.57$. The error in these measurements are dwarfed by the diameter ranges of the organisms and would have no substantial effect on the final acoustic comparisons.

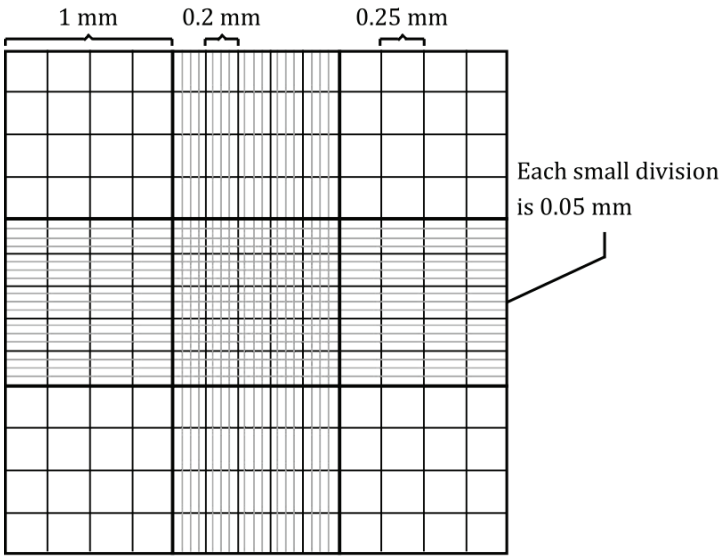


Figure 3.4: Improved Neubauer haemocytometer schematic. Grid spacings are labelled.

Using this scaling factor, all dimensions of *S. palmeriana* were adjusted to their expected true values. These are the dimensions reported in the thesis (Figures 3.5 through 3.8). Additionally, reviewing the metadata of the micrographs from the other studied species, it was confirmed that they share the same initial calibration factor. Thus, the corrective factor found for *S. Palmeriana* was applied to all species.

Confidence in the results returned from this corrective scaling factor is reaffirmed by the similarity of the new dimensions dimensions to those already published using the same stock cultures (*MacIntyre and Cullen*, 2016; *MacIntyre et al.*, 2018) and from additional literature on the same species (*Hasle and Syvertsen*, 1997).

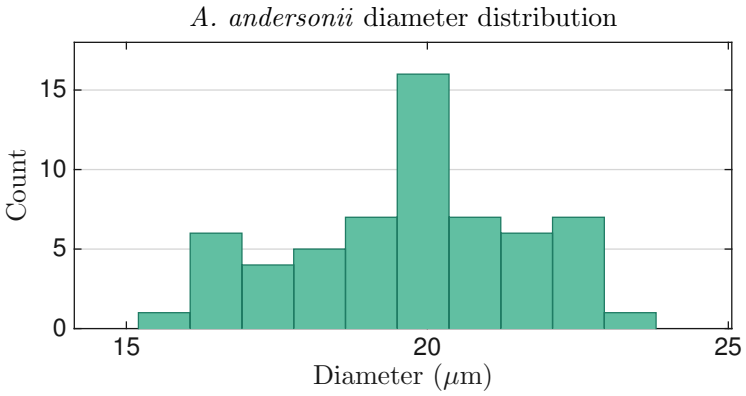


Figure 3.5: *A. andersonii* diameter distribution

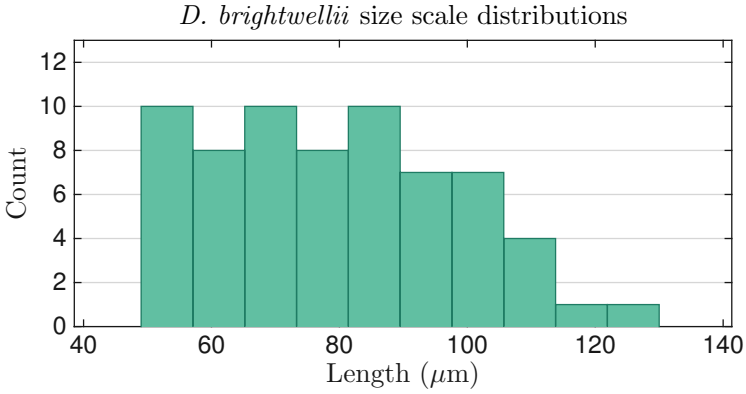


(a) Length distribution

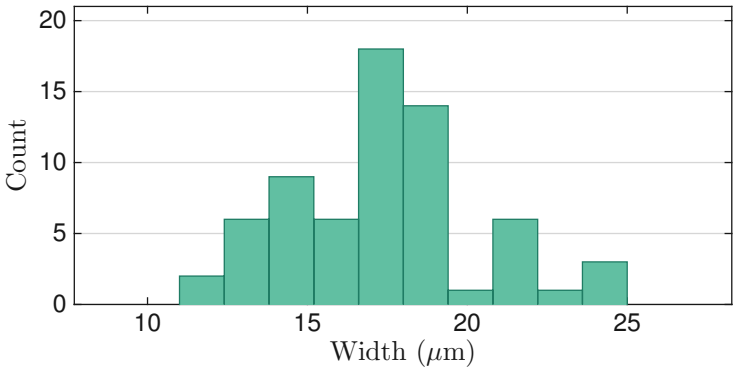


(b) Width distribution

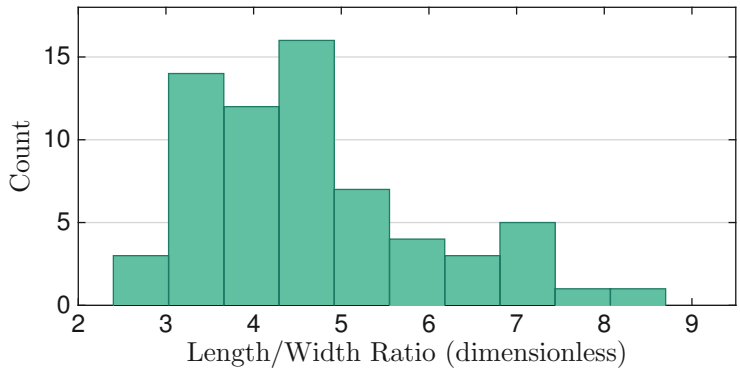


(c) Length-to-width distribution

Figure 3.6: *D. brightwellii* size scale distributions. (a) Length distribution. (b) Width distribution. (c) Length-to-width distribution.

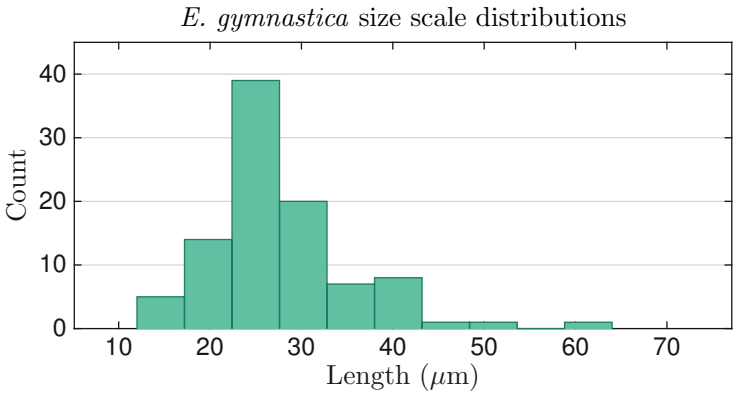


(a) Length distribution

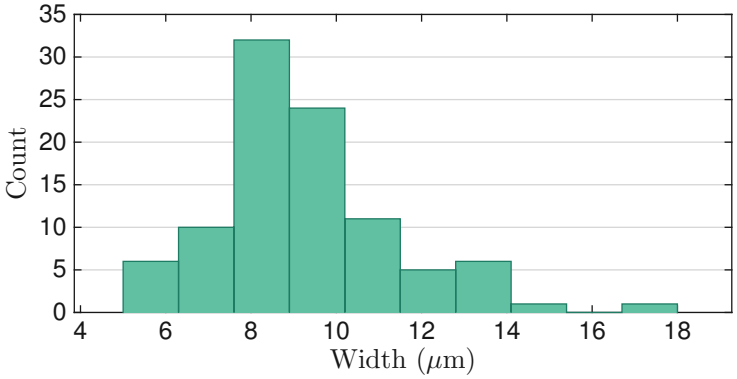


(b) Width distribution

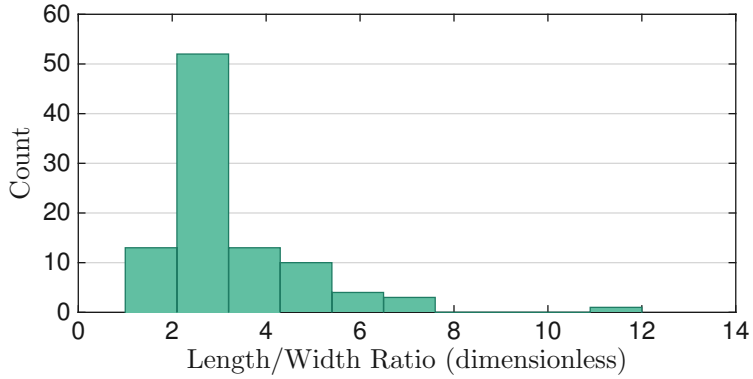


(c) Length-to-width distribution

Figure 3.7: *E. gymnastica* size scale distributions. (a) Length distribution. (b) Width distribution. (c) Length-to-width distribution.

*S. palmeriana* size scale and total chain length distributions

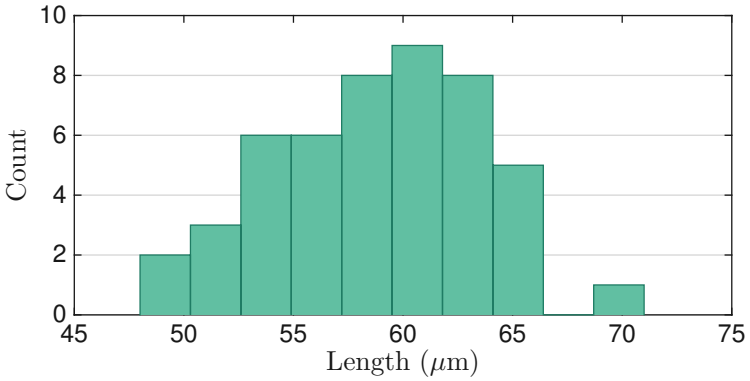


(a) Length distribution

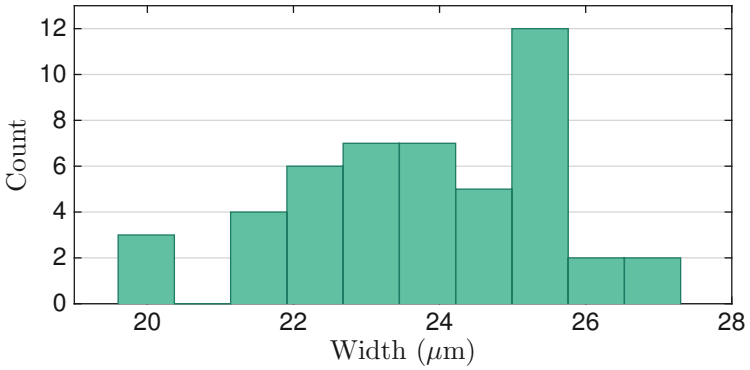


(b) Width distribution

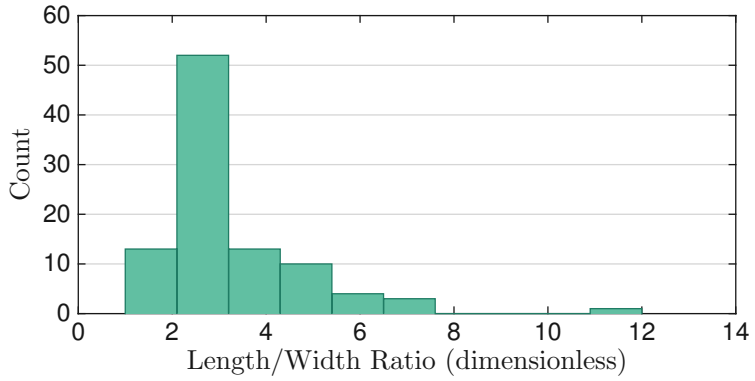


(c) Total chain-length distribution

Figure 3.8: *S. palmeriana* size scale and chain-length distributions. (a) Length distribution. (b) Width distribution. (c) Chain-length distribution.

## 3.3 Observing Backscatter from Phytoplankton

Acoustic observations of each species began once they reached a stationary growth phase. At this point, the tanks were placed under the flow hood, opened, and the acoustic apparatus submerged (see Figure 3.9.) The initial observations were collected at this maximum concentration and are referred to as the *1.0 dilution* tests. Samples used for the biological measurements detailed in Section 3.2 were taken coincident with each acoustic test.

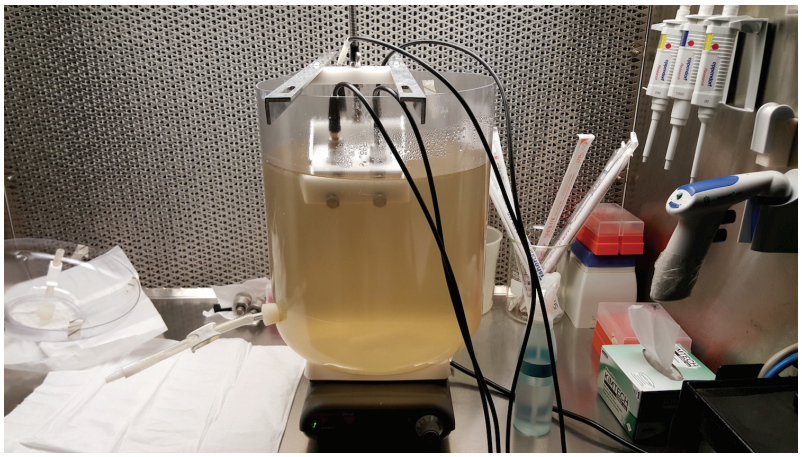

Figure 3.9: The 20 L test tank photographed during acoustic measurements of *A. andersonii*. The instrument is suspended across the top of the tank with the transducers submerged just below surface. The transducer pair that is being tested is positioned towards the center of the tank.

Each acoustic test consisted of transmitting 100 individual pings separated by 500 ms for each transducer pair and recording each ping for a total of 1 ms (including the full ping length). The ping delay of 500 ms was chosen following a correlation test with more rapid echo soundings. A lag of 500 ms was found to be sufficient to produce non-correlated returns – allowing for a non-biased mean analysis of the 100 pings per test.

The pings used were linear frequency-modulated chirps (or sweeps) that covered approximately an octave bandwidth around each transducer's center frequency. Two chirp lengths were used throughout the experiment with the anticipation of selecting the best (i.e. highest signal-to-noise ratio) in the future. The first to be transmitted was labelled *short* with a length of 150 µs. The second, labelled *long*, had a length of 300 µs. During analysis,

it was found that the $300\,\mu s$ signal was a more appropriate choice and used exclusively onward. Sample rate for both transmitting and receiving was set to 50 MHz, exceeding the necessary Nyquist frequency for the signals used. During the study of the first two species, a 10 MHz transducer was used. Regrettably however, limitations of the amplification equipment used did not allow further study at these frequencies.

Following the initial *1.0 dilution* test, observations of backscattering at decreasing concentrations were conducted (see Table 3.2 for details). For each dilution, culture was drained and disposed of in a bleach solution before going into a waste container. The volume was increased back to 15 L using seawater filtered through a $1\,\mu m$ filter. While the seawater likely lacks the necessary nutrients for continued growth, or even to maintain the culture, it was expected that over the course of acoustic measurements that it would have relatively little to no impact on the culture in regards to their scattering physics (i.e. morphologies remained unchanged.) This was later confirmed by the micrograph images, showing no change to the organism morphologies.

Table 3.2: Listing of the dilutions measured for each species. Being the first species studied, *D. brightwellii* differs from the others since its dilutions were arbitrarily selected. The later dilutions were calculated based on simple values for water volume transfers between for each dilution (e.g. 500 mL, 2 L, etc)

| **Species** | **Dilutions - (total count)** |
|---|---|
| *Alexandrium andersonii* | 1.0, 0.871, 0.743, 0.614, 0.486, 0.357, 0.229 - (7) |
| *Ditylum brightwellii* | 1.0, 0.900, 0.800, 0.700, 0.600, 0.500, 0.400, 0.300 - (8) |
| *Eutreptiella gymnastica* | 1.0, 0.871, 0.743, 0.614, 0.486, 0.357, 0.229 - (7) |
| *Stephanopyxis palmeriana* | 1.0, 0.871, 0.743, 0.614, 0.486, 0.357, 0.229 - (7) |

### 3.3.1 Data Pre-Processing

The raw scattering data are not ideal for in-depth analysis: they are noisy, muddied with extraneous frequencies, and not focused on the target region. For the purposes of in-depth analysis, the initially noisy raw acoustic data were filtered and time-gated to appropriate

limits. The steps taken from a raw time-series to final are, in order, (1) bandpass filter, (2) pulse compression, and (3) time-gating.

**Bandpass Filter** A 5th-order Butterworth bandpass filter is applied. Limits of the bandpass are shown in Table 3.3 and graphically in Figure 3.10. The limits of the bandpass were selected intentionally as to not taper or limit the chirp content in any way. By applying the filter, extraneous frequencies are reduced or eliminated altogether.

**Pulse Compression** A matched filtering technique known as pulse compression is used to reduce noise as well as to compress the chirped signals into highly-localized peaks. The reduction of noise is accomplished by pulse compression by cross-correlating the transmitted signal with the returned time-series, thereby amplifying received signals with the same waveform while reducing anything else, thereby increasing the signal-to-noise ratio. Strong, singular reflections, such as that from the bottom of the tank, are transformed from their lengthy chirp representation to a well-defined peak at the first moment the reflection is received. The application of the pulse compression technique for acoustic data follows the details provided in *Chu and Stanton* (1998) where it can be reviewed in more detail.

**Time-gating** Because of the geometry of the transducers in the apparatus, a focus occurs where the two beam patterns intersect. The scattered signal is expected to be strongest in this region. The focal distance of the transducers was first found by physically measuring the point of intersection. By reviewing the time-series, an increased amplitude corresponds to this distance and is interpreted as a confirmation of the first measurements. These data are subsequently time-gated around this focal point $\pm 0.35$ s for an observational range of 0.15 to 0.21 ms. This range was selected in order for the upper limit, 0.21 ms, to remain below the measurable sidelobe artifacts of the bottom reflection post pulse-compression (most noticeable in the 1

MHz dataset in Figures 4.1-4.4.)

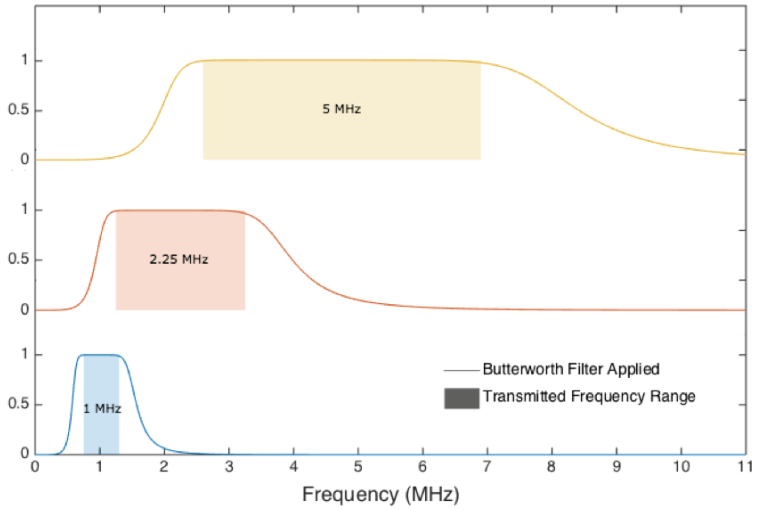


Figure 3.10: Graphical representation of the Butterworth bandpass filters being used.

Table 3.3: Transducer chirp frequency range and their corresponding Butterworth bandpass limits.

| **Transducer Center Frequency (MHz)** | **Chirp Frequency Range (MHz)** | **Butterworth Band-pass Filter Range (MHz)** |
|---|---|---|
| 1.00 | [0.75, 1.30] | [0.60, 1.50] |
| 2.25 | [1.25, 3.25] | [1.00, 3.70] |
| 5.00 | [2.60, 6.90] | [2.10, 7.90] |

Following pre-processing, the signals were then converted to their corresponding frequency domain by applying a Fourier transform and were calibrated using the frequency dependent coefficients shown in Figure 3.11. The calibration method is detailed below.

### 3.3.2 Calibration

Calibration of the acoustic system was completed in a different cube-shaped tank with side lengths of 60 cm. The tank's larger size allowed greater maneuverability when manipulating the calibration spheres and the acoustic apparatus. Different calibration methods were used for the 1 MHz transducers and the 2.25 and 5 MHz transducers.

The 1 MHz transducers were calibrated using a 9.5 mm diameter tungsten carbide (WC) sphere mounted at the end of a 0.75 mm diameter cylinder rod (seen at the bottom of Figure 3.1). The rod is oriented to be attached on the reverse side of the transducer focusing area. Conceptually, it can be considered to be in the acoustic 'shadow' of the transmitted pressure wave. Any additional scattering introduced by the rod was seen to be negligible compared to the primary scattering from the sphere. The calibration curves shown in Figure 3.11 were calculated following the methods presented in *Lavery et al.* (2009). The theoretical models were parameterised using a compressional WC soundspeed of 7286 m/s and a shear soundspeed of 4154 m/s, and water soundspeed of 1500 m/s with a scattering angle of $25^o$. The WC soundspeed parameters were selected from *Dourado* (2015) where a sensitivity analysis was conducted on a similar WC sphere. A problem with broadband calibration with a target spheres is the inherent resonances, or nulls, in the final curve that dramatically increase uncertainty at their location. However, in my tests, the nulls were not excessively deep and so no further processing was completed.

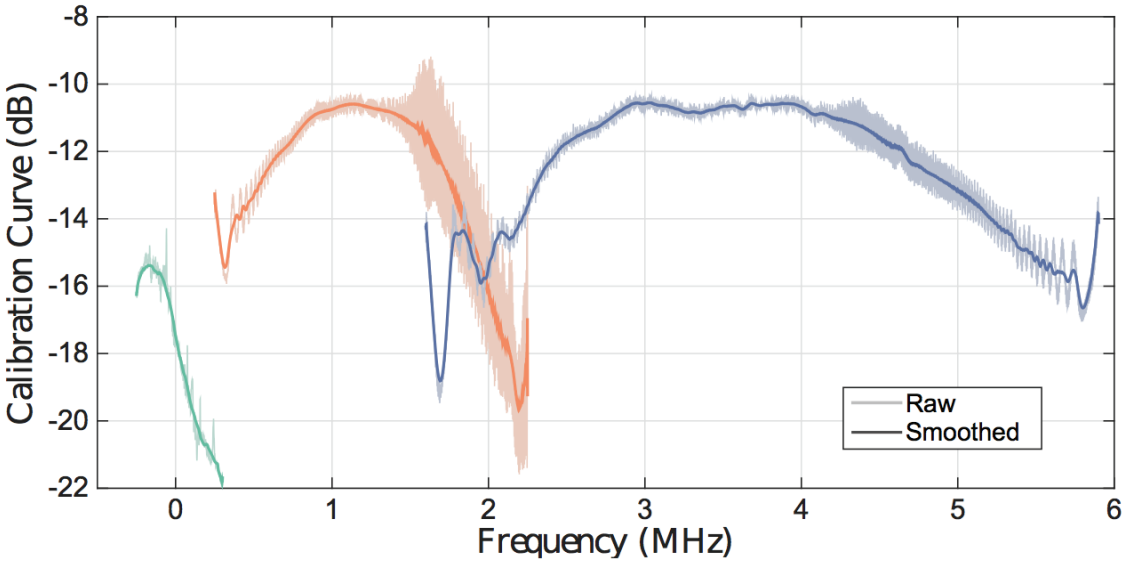


Figure 3.11: Calibration curves for the three transducer pairs found using a 9.5 mm diameter tungsten carbide (WC) sphere. The first transducer pair, centered on 1.0 MHz, utilized a full-reflection in calculating the calibration curve whereas the other two utilized only the front-interface reflection.

The 2.25 and 5.0 MHz transducers were calibrated instead using the WC sphere suspended using stretched cellophane. This method was used after inaccurate results were found when using the sphere and rod setup for calibration. It is likely that the rod was now observed at these higher frequencies, introducing complexity in the scattered wave that couldn't accurately be accounted for with simple calibration models. Calibration curves were calculated using the same methods as for the 1 MHz pair except that a partial-wave analysis that only considered the front-interface reflection (*Stanton and Chu*, 2008) was used. With this method, nulls introduced by the full-wave description from secondary and tertiary scattering phenomena do not affect the final calibration. A rigid sphere model (using equation 2.7 with $g$ and $h$ going to infinity) was used to calculate the front-interface reflection and was parameterised with a water soundspeed of 1500 m/s and a scattering angle of $25^o$.

### 3.3.3 Calculating a Mean Volume-Scattering Strength

After correction using the calibration curves, the sets of 100 pings were averaged to obtain a single curve for analysis. Due to the observed minimal coherence between consecutive pings, the scattering intensities follow a Rayleigh distribution (*Medwin and Clay*, 1998). Therefore, by using MATLAB's *raylstat* function, a Rayleigh mean was calculated along with the corresponding 95% confidence interval, which results in a characteristic spectrum for each particular species over the range of measured frequencies.

These spectra, however, were noisy and it was anticipated that they would be difficult to accurately compare to models without some level of smoothing. To accomplish this, a moving-average filter is applied with a bin-width of 20 kHz.

The result; an ensemble averaged, smoothed, volume-scattering strength is shown for *A. andersonii* in Figure 3.12 by the combination of the dark and light green curves. The natures of the light and dark green curves are explained in the following subsections.

### 3.3.4 Acoustic Uncertainty Estimation & Bootstrapping

Underwater acoustical data is susceptible to uncertainty, so I made a strong effort to source, propagate, and quantify uncertainty in my analysis of phytoplankton backscatter. The primary sources of uncertainty resulting from my processing comes from the confidence interval from calculating a mean scattering intensity and the binning uncertainty from applying a moving-average to smooth the individual spectra. The uncertainties for the phytoplankton scattering and calibration are calculated independently and later combined, following traditional error propagation methods, to give a total uncertainty in the volume-scattering strength. It should be noted that this level of error propagation has not been done in past acoustic studies of phytoplankton.

The total uncertainty in the volume-scattering strength is illustrated for *A. andersonii* by the light green shaded area in Figure 3.12.

A secondary uncertainty analysis utilizing the bootstrapping method (*Efron and Gong*, 1983) was conducted following the comparisons of $S_v$ spectra to the various scattering models. The bootstrapping method was applied by randomly sub-sampling the 100 pings, with replacement, to produce a new set of 100 pings. By allowing for replacement, the new set of pings would likely have repeated entries and would omit some pings all-together. These pings would then follow the same pre-processing methods, calibration, averaging and smoothing as the original set. This new $S_v$ was then compared to models parameterized with the best-fit coefficients found as described in Section 3.4. This process was repeated 100 times to produce a set of goodness-of-fit parameters unique to each sub-sampled ping set. The variance of this set was found to be nominally low, less than 10% of the mean. This low variance gives confidence in the assumptions of non-coherence and a Rayleigh distribution of scattering amplitudes and strengthens the accuracy in model-fit conclusions.

### 3.3.5 Background Measurements

In order to determine a noise floor, background measurements were recorded in a test tank filled with only seawater. The resulting $S_v$ curves can been seen in Figure 3.12. As expected, the noise floor, in red, varies with frequency. It can also be seen at some frequencies to exceed the measured mean volume-scattering strength from the *A. andersonii* culture shown by the combination of dark and light green curves.

The curves are divided into the dark and light curves to indicate the data that have been used in model comparisons (dark) and those that have been neglected due to lack of confidence (light). Regions of confidence include data whose errors exceed the noise floor in addition to where the calibration coefficient is within the half-max value. Regions with reduced confidence include data that don't satisfy both of those conditions simultaneously for a given frequency. The noise curve has been omitted from all further plots for clarity.

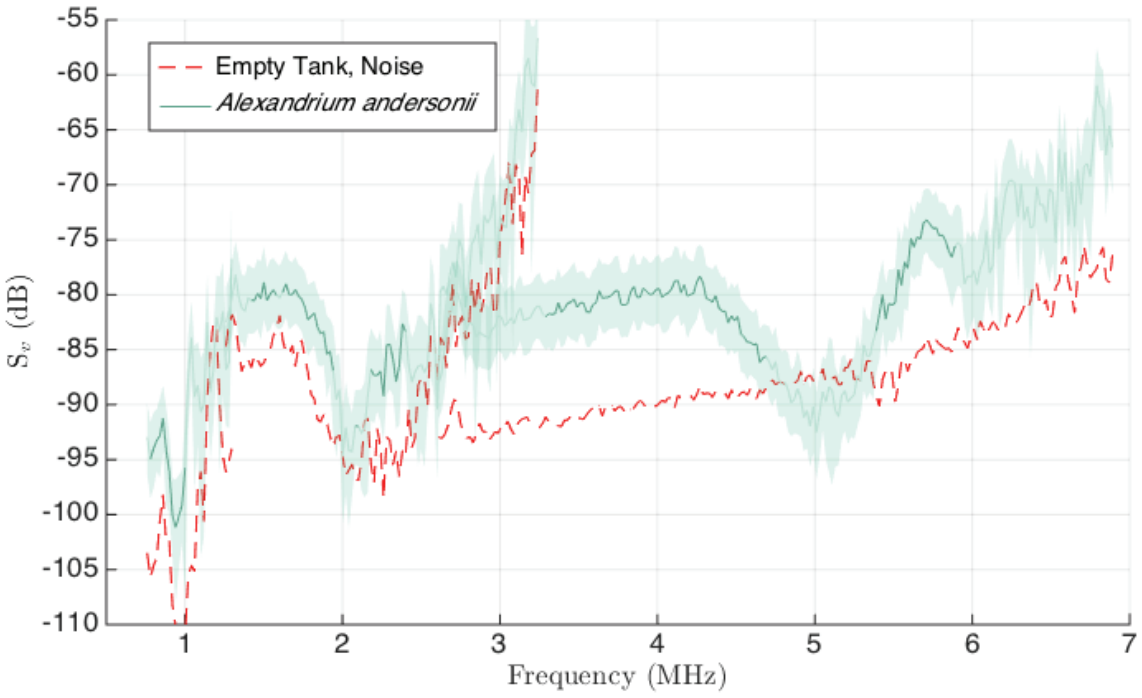


Figure 3.12: Background noise recorded from an empty tank providing a noise floor for measurements. *A. andersonii* volume-scattering strength is shown to illustrate the relative signal-to-noise ratio across the studied bandwidth. Data whose error (shaded, light green) exceeds the noise floor and is within the half-max of the max calibration coefficient value for each transducer pair are shown in dark green.

## 3.4 Acoustic Model Comparisons

Backscattering results from each test species are compared to their exemplar models given in Section 2.4. Only data that meet the criteria described in Section 3.3.5 (i.e. dark green curves in the given example figure) and their corresponding errors are compared to the models. The lengths used in the models are those measured from the micrographs and presented in Figures 3.5 through 3.8. A model for any given composition parameterisation is run for each length measurement and an average is taken at the end to give a representative model fit. An iterative search for the best-fit model is done by varying their composition parameterisation. In the application of the fluid sphere, fluid prolate spheroid, and fluid cylinder models, their $g$ and $h$ values are varied. When applying a fluid-filled shell model, two different approaches are taken: (1) assume a shell $g$, $h$ and $v_{shear}$ estimated from the literature for the corresponding material (silica for *D. brightwellii* and cellulose for *A. andersonii*) and then vary the interior fluid's $g$ and $h$ and (2) assume a fluid interior $g$ and $h$ estimated from the literature and then vary the shell parameters mentioned above.

An initial guess of the variable parameters is made based on the literature and then expanded to 64 equally spaced values between 0.2 and 4 times the initial guess. Models are run and fitted to observations using the root-mean-squared (RMS) difference metric described in Section 3.4.1. The parameters that produce the lowest RMS difference for a given model are taken to be the best-fit. These values are taken as the next best-guess in the iterative search and the parameter range is narrowed by one-half. Iteration continues in this fashion until a set of at least 10 RMS values fall within 10% of the lowest (best-fit) result. This produces the reported best-estimate value for organism characteristics and a possible range of values.

When reporting which model best describes the scatter of an organism, the lowest RMS value is considered first. However, there are cases where biologically-unrealistic parameterisation values produced the best fits. These cases are addressed individually in

the discussion section.

### 3.4.1 Root-mean-squared Goodness of Fit

To compare the spectra to their respective models and to find the best fit, I used the root-mean-square (RMS) deviation as a metric,

$$\text{RMS} = \sqrt{\frac{\sum w(y - y_{model})^2}{\sum w}} \tag{3.1}$$

where $y$ is the $S_v$ spectra and $y_{model}$ is the model being tested against. I have also included a weighting term, $w$, given by the inverse of the relative error at each frequency as calculated in Section 3.3.4. By this formulation, regions of higher confidence are weighted higher (given more importance) than those with less confidence. A lower RMS value indicates a more accurate fit.

# CHAPTER 4

# BACKSCATTER FROM PHYTOPLANKTON

This chapter details the acoustic backscatter results obtained from the experiments with the various phytoplankton species. In addition to the raw returns, I provide the dilution test series and then the spectra including volume scattering strengths, the best-fit model results and the corresponding fit parameters describing the organism's density and sound speed contrast. Lastly, an unexpected peak in the scattering return is compared to a bubble scattering model in an effort to explain and characterize it.

## 4.1 Detecting Different Phytoplankton Species

One of the objectives (Section 1.1) of this study was to simply determine if it was possible to detect phytoplankton species with different morphologies at these size scales. To accomplish this, the acoustic scattering time series of each species is compared to the relative noise floor of each transducer. It can be assumed that any signal exceeding the noise floor must be due to scattering off of objects within the water column. In the case of ideal mono-culture growth, it follows that the signal is scatter from the phytoplankton. The time series comparisons can be seen in Figures 4.1 through 4.4.

The figures are sorted by species with each individual panel showing backscatter data from a particular transducer (1.0 MHz at the top, 2.25 MHz in the middle, and 5.0

MHz at the bottom). These data have been band-pass filtered and pulse compressed in order to reduce the noise as well as to compress the strong bottom reflection into a comparatively narrow peak. By compressing the bottom reflection, clarity is improved in all other regions of the scattered return, especially at the focal point, approximately $14\,\mathrm{cm}$, or $0.18\,\mathrm{ms}$ (two-way travel time) away.

Plotted in gray are all 100 individual pings over-layed on top of each other (giving the appearance of a solid region in the background.) To highlight the contribution of individual pings, two have been arbitrarily selected and plotted in orange and purple. Lastly, a mean noise floor for each transducer has been plotted in red.

The time axes of all the figures have been reduced to a region surrounding the calculated focus of the bi-static transducers. The scattering volume around the focus will coincide with the most accurate (and highest level of) backscatter. The amplitude axes are shown as the envelope of the compressed pulse and are uncalibrated. There is no need to apply a calibration in these comparisons as both the phytoplankton backscatter and noise floor returns would be affected equally and the only goal in this part of the analysis is to look at the relative amplitudes of each.

In all the panels the bottom reflection is easily identified at the trailing end of the gated time series ($\sim t = 0.26$ ms). It is most prevalent in the 5.0 MHz panels where it is very narrow, following from the inverse relationship to bandwidth length (*Chu and Stanton*, 1998). Otherwise, the noise floor is relatively constant with variation mostly coming from the sidelobes of the bottom reflection peak, an effect of the pulse compression calculation.

These figures show that the majority of the backscatter return exceeds the noise floor within the focus region. It is most obvious when looking at the overlayed pings in gray, or alternatively, at the individual ping traces (particularly noticeable in Figures 4.1a and 4.3b). As you move away from the focus, the phytoplankton observations fall off considerably to match the noise floor, as expected. It should be noted that there are regions within the focus where observations do fall below the noise floor slightly. These

are addressed in the frequency domain analysis in the following section.

One particular case that needs to be mentioned is that of the 5 MHz return of the chain-forming *S. palmeriana*, shown in Figure 4.4c. Compared to the other species at this frequency, there is a markedly lower return in the focus region and significantly fewer peaked features. The limited scattering amplitude can be seen again in its corresponding spectrum in Figure 4.10. Being a regular chain-forming organism, the morphology of this species sets it apart from the others tested in this study. A long length-to-width ratio due to the joining of anywhere from 2 to 14 individual cells (see Figure 3.8c) produces a varied scattering surface dependent on their orientation. A biased orientation due to latent vorticity after mixing between insonification tests could also compound the effect to decrease scattering amplitudes if the chains aligned their short edges with the acoustic beam, limiting the broad side to contribute only to secondary scattering interactions. Although scattering is quite weak in the focal range ($\sim 1.8 \times 10^{-4}$ s) for all three frequency ranges, its unclear from just the time-series if all three were detecting only noise. Therefore, more discussion involving the spectrum is presented in Section 4.4.4.

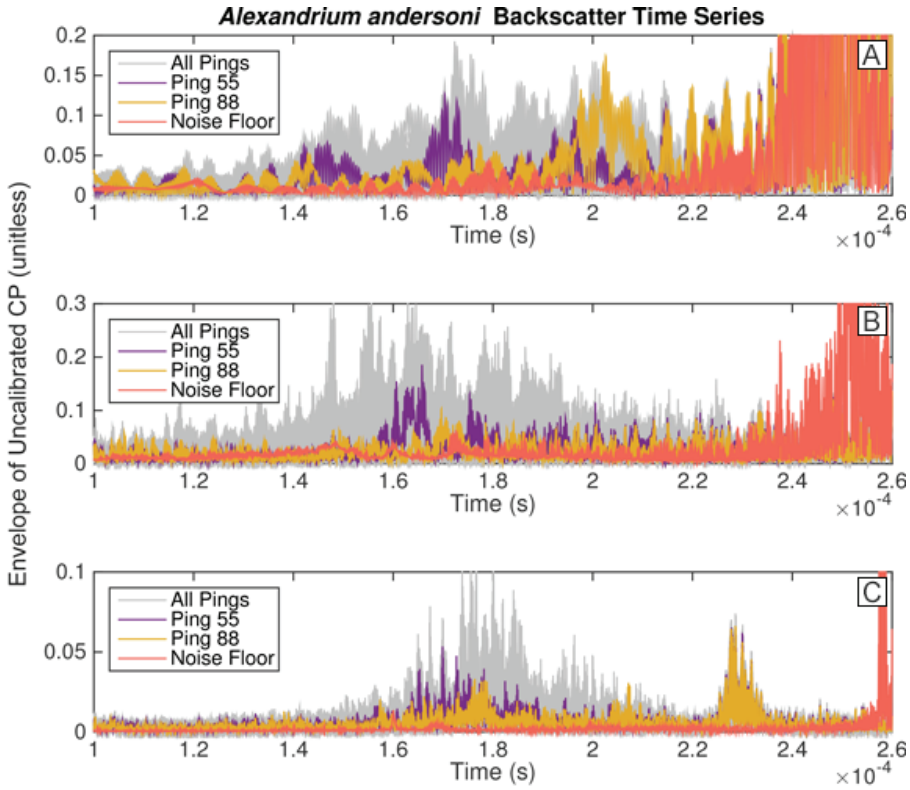


Figure 4.1: *A. andersonii* backscatter timeseries showing the uncalibrated envelope of the compressed pulse. (a) 1.0 MHz transducer tests. (b) 2.25 MHz transducer tests. (c) 5.0 MHz transducer tests.

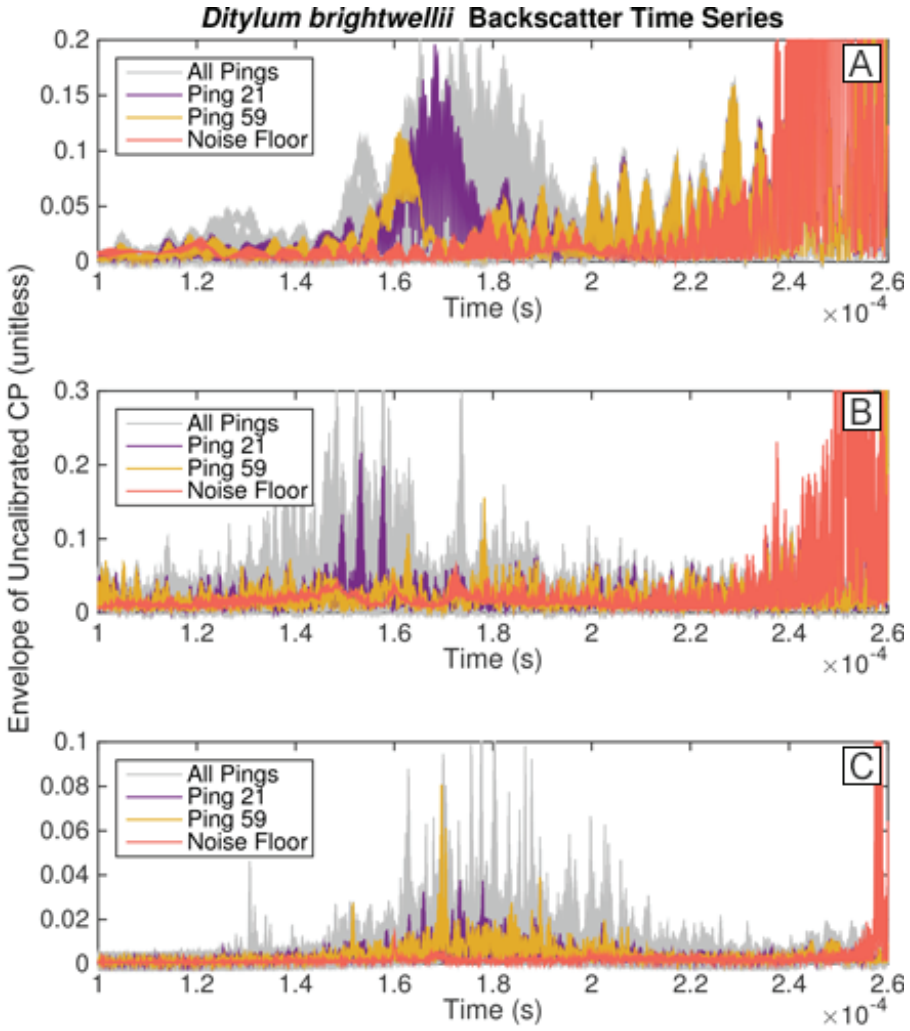


Figure 4.2: *D. brightwellii* backscatter timeseries showing the uncalibrated envelope of the compressed pulse. (a) 1.0 MHz transducer tests. (b) 2.25 MHz transducer tests. (c) 5.0 MHz transducer tests.

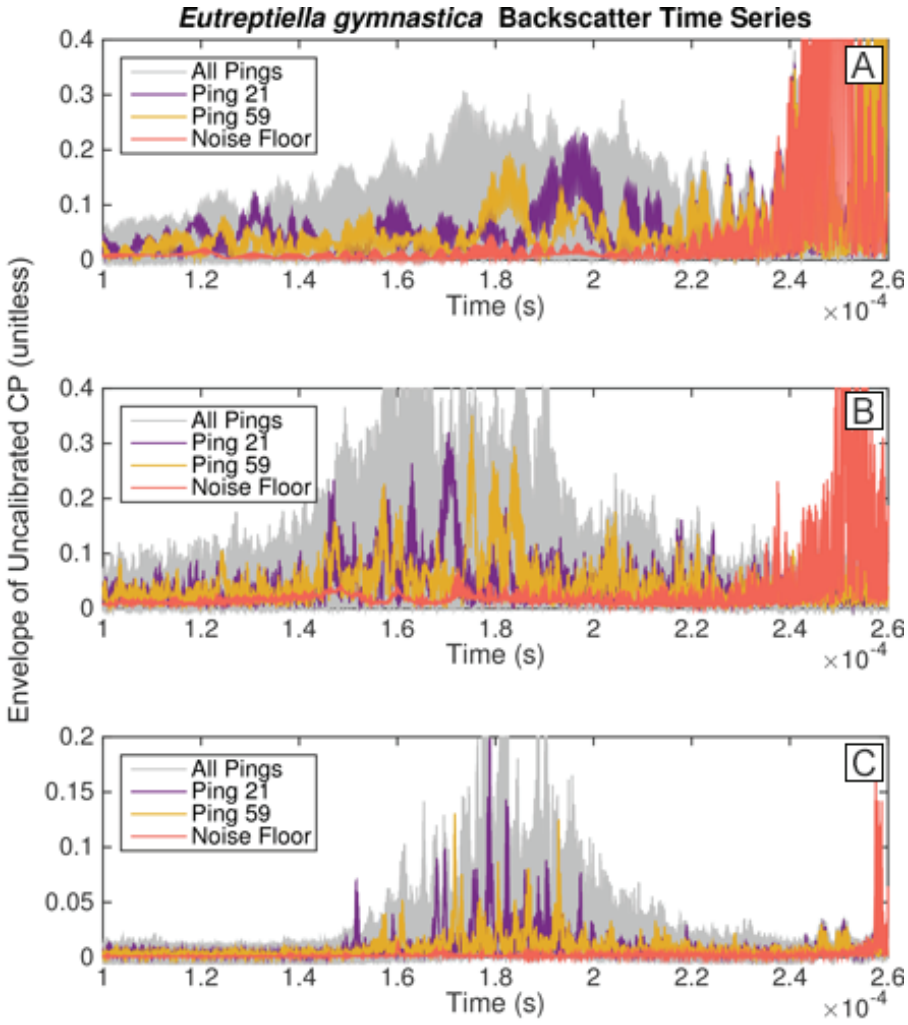


Figure 4.3: *E. gymnastica* backscatter timeseries showing the uncalibrated envelope of the compressed pulse. (a) 1.0 MHz transducer tests. (b) 2.25 MHz transducer tests. (c) 5.0 MHz transducer tests.

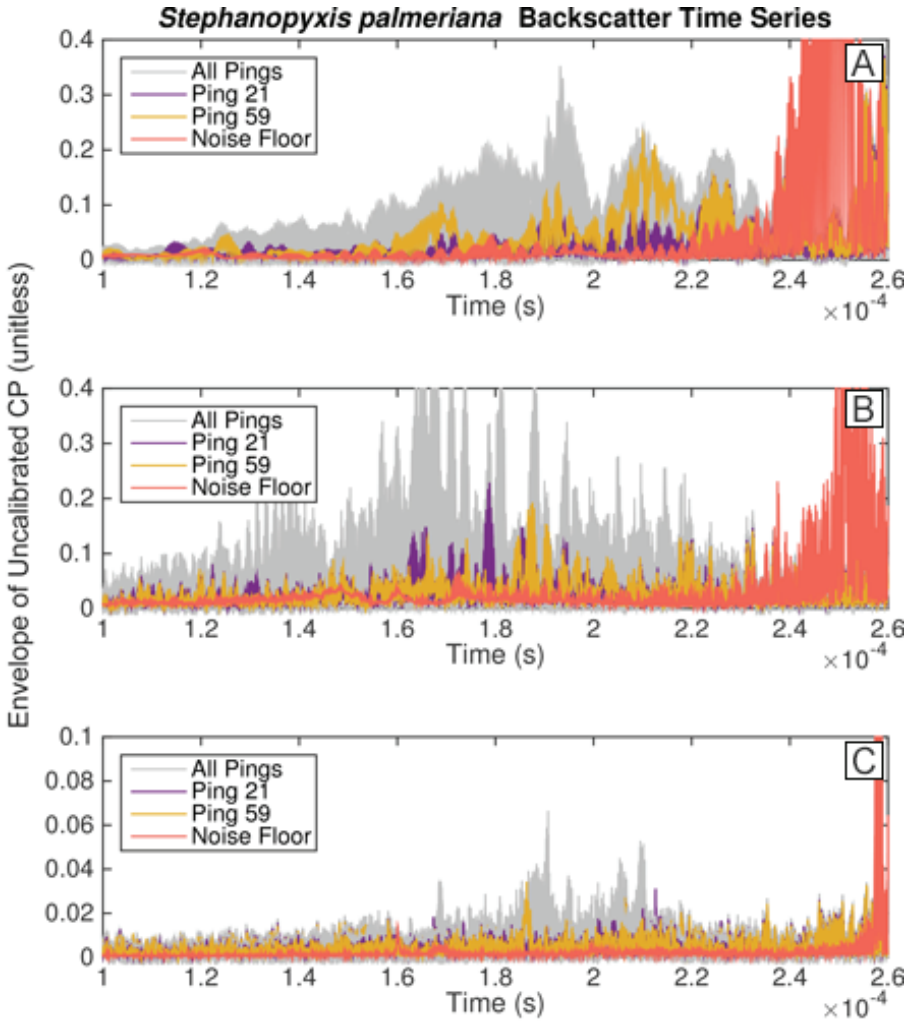


Figure 4.4: *S. palmeriana* backscatter timeseries showing the uncalibrated envelope of the compressed pulse. (a) 1.0 MHz transducer tests. (b) 2.25 MHz transducer tests. (c) 5.0 MHz transducer tests.

## 4.2 Dilution Tests

As part of this study, each species was insonified at multiple decreasing concentrations (see Table 3.2) The maximum concentrations (1.0 dilution) for these species were $1.22 \times 10^{10}$, $5.31 \times 10^{9}$, $3.52 \times 10^{10}$ and $5.56 \times 10^{9}$ individuals/m$^3$ for *A. andersonii*, *D. brightwellii*, *E. gymnastica*, and *S. palmeriana* respectively. Analysing the dilution series results can provide insights on two fronts: (1) they can confirm the conclusions from Section 4.1 that the individual cultures were measured and (2) provide a lower detection limit if

the amplitudes for each decreasing concentration begin to diverge from the expected curve. In support of (1), if the observed scattering intensity falls linearly with decreasing concentration, there is confidence that you are observing the physical dilution change of scattering objects (the phytoplankton). As for (2), as the concentration of phytoplankton decreases, it will eventually hit a possible-observation limit (i.e. noise floor.) Once it reaches this threshold, the scattering intensity will taper from a linear decrease and flatten – all variation at this point would be due to stochastic noise.

To determine the relative scattering intensities for each species against their initial (presumed maximum) concentration, the square of the compressed-pulse time-series envelope (shown in Figures 4.1 through 4.4) is averaged for each ping across the time-gated region between 0.15 and 0.21 ms, whose center is approximately the acoustic focus, and then averaged across all 100 pings. The range of the gating was selected in order to maximize the contained energy without including any side-lobe artifacts from the compressed-pulse of the bottom reflection. This is done for each transducer pair to produce an individual value for every species, centre frequency and concentration. Each result was then normalized to the initial concentration observed (the 1.0 dilution.) These data are plotted in Figure 4.5 alongside the expected concentration curve (a 1:1 line) and a corresponding linear regression.

*Stephanopyxis palmeriana* has been excluded from these figures. When analysing the results for decreasing concentrations, it was found that the average intensity increased by an order of magnitude for the 0.871 dilution compared to the 1.0 dilution and then remained approximately constant as the concentrations decreased. Reviewing the lower concentration time-series, it was noted that the increased intensities corresponded with substantially higher background noise than the initial 1.0 relative concentration observations. This species is discussed further in Section 4.4.4.

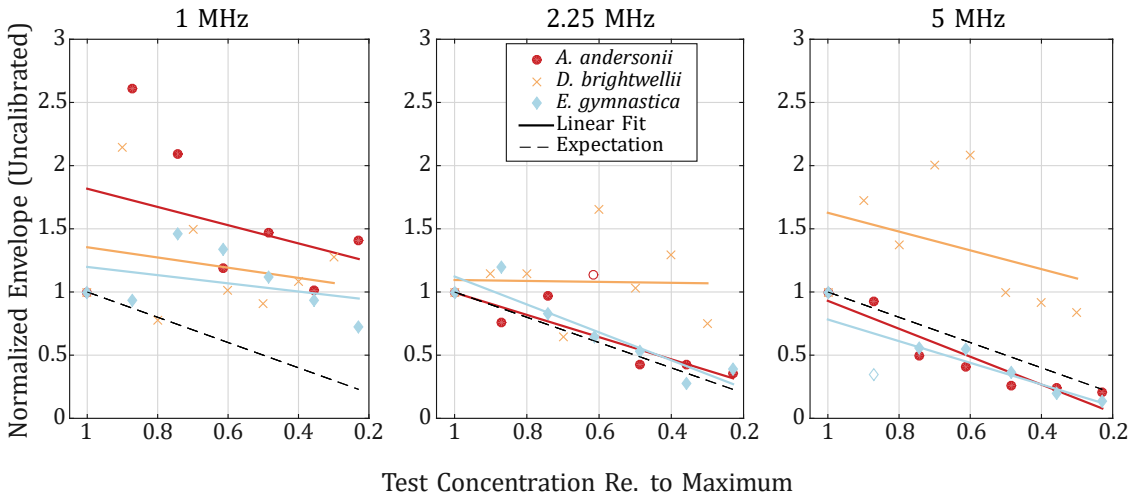


Figure 4.5: Concentration dependence of observed scattering. The normalized envelope of the pulse-compressed scattering intensity from the focal region of the transducers is plotted as a function of dilution of the phytoplankton sample. Only the three species with the strongest signal to noise ratio are shown. The normalized envelope is expected to scale directly with dilution if the primary source of the acoustic return is the phytoplankton (and not noise), thus the dashed line indicates a 1:1 relationship. Regression results are tabulated in Table 4.1. Note: unfilled data points indicate that it was not used during regression due to an anomalous magnitude.

These data from the remaining species are noisy, but they do behave with some regularity in the higher frequencies. Starting with the panel for 1 MHz, all three species can be seen diverging from the expected concentration curve relatively quickly, if not immediately at the 1.0 concentration. From the linear regression (Table 4.1), it can also be seen that all three do not follow the expected dilution curve slope. Additionally, the calculated $R^2$ values were 0.11, 0.05, and 0.13 for the species in descending order in the legend – suggesting poor fits, and that the observations were primarily noise. However, this analysis, of course, depends on the assumed accuracy of the 1.0 dilution measurement in regards to normalization. To account for a possible false measurement, a regression (not reported in the table) was completed while ignoring the first data point of all the species and additionally ignoring the second for *E. gymnastica*. Results for the first two species were similarly poor and comparable to their previous regressions. However, the regression for *E. gymnastica* with the first two data points ignored returned a slope of precisely 1.00

Table 4.1: Dilution test series regression results.

| **Frequency (MHz)** | **Species** | **Regression Results** | |
|---|---|---|---|
| | | Slope | $R^2$ |
| 1.00 | *A. andersonii* (●) | 0.72 | 0.11 |
| | *D. brightwellii* (×) | 0.40 | 0.05 |
| | *E. gymnastica* (♦) | 0.32 | 0.13 |
| 2.25 | *A. andersonii* (●) | 1.00 | 0.83 |
| | *D. brightwellii* (×) | 0.04 | 0.00 |
| | *E. gymnastica* (♦) | 1.10 | 0.85 |
| 5.00 | *A. andersonii* (●) | 1.10 | 0.87 |
| | *D. brightwellii* (×) | 0.74 | 0.13 |
| | *E. gymnastica* (♦) | 1.11 | 0.96 |

with an $R^2$ of 0.99 suggesting an impeccable correlation to the expected curve. With that being said, the removal of the two highest concentrations (whose observation would be expected to be the most accurate) was necessary and this level of precision is not seen even in the higher frequencies where a noise floor also appears to have been reached. Because of these reasons, I ultimately do not have confidence in this regression. Altogether, confident observation of these species at these concentrations at 1 MHz is unlikely.

Moving to the $2.25\,\mathrm{MHz}$ tests, *A. andersonii* and *E. gymnastica* and their regressions follow the expected curve with slopes of 1.00 and 1.10 with calculated $R^2$ values of 0.83 and 0.85 respectively. One data point (unfilled red marker) of *A. andersonii* at a 0.614 relative concentration was removed in the final calculation due to its distance from the initial regression and the continued regular behaviour of observations below that concentration. Because of the relatively high $R^2$ and accurate fitted-slope, there is a high likelihood that I am observing these species at these frequencies at at these concentrations.

Applying the regression to the observations with removal of the lowest concentrations did not alter the regression result of either species. The regression performance of *D. brightwellii* continues to be poor in these frequencies with near horizontal slope and an $R^2$ of 0, explaining none of the variability observed.

Lastly, the $5\,\mathrm{MHz}$ results share similar characteristics with the $2.25\,\mathrm{MHz}$ tests. Both *A. andersonii* and *E. gymnastica* perform well again in their linear regressions returning slopes of 1.10 and 1.11 with $R^2$ values of 0.87 and 0.96 respectively. Similar to the previous frequency set, one data point (unfilled blue diamond) of *E. gymnastica* at a 0.871 relative concentration was rejected in the final regression following an initial test. Additionally, marginal change occurred in the regression when removing the lowest concentrations observed. Therefore, there is reasonable confidence that these species are being observed at 5 MHz at these concentrations. In the case of *Ditylum brightwellii*, observations do not improve at these higher frequencies with markedly low $R^2$ values returned regardless of which concentrations are included in the regression.

Ultimately, from these dilution tests, it suggests that both *A. andersonii* and *E. gymnastica* can be confidently detected down to relative concentrations of at least 0.229 (equivalent to $2.794\times10^9$ individuals/m$^3$ and $8.061\times10^9$ individuals/m$^3$, respectively) with frequencies of $1.25\,\mathrm{MHz}$ up to $6.90\,\mathrm{MHz}$ (and likely, higher). Due to the poor regression results across all frequencies with *D. brightwellii*, it is likely not being observed with accuracy in this experiment.

## 4.3 Volume Scattering Strengths and Spectral Features

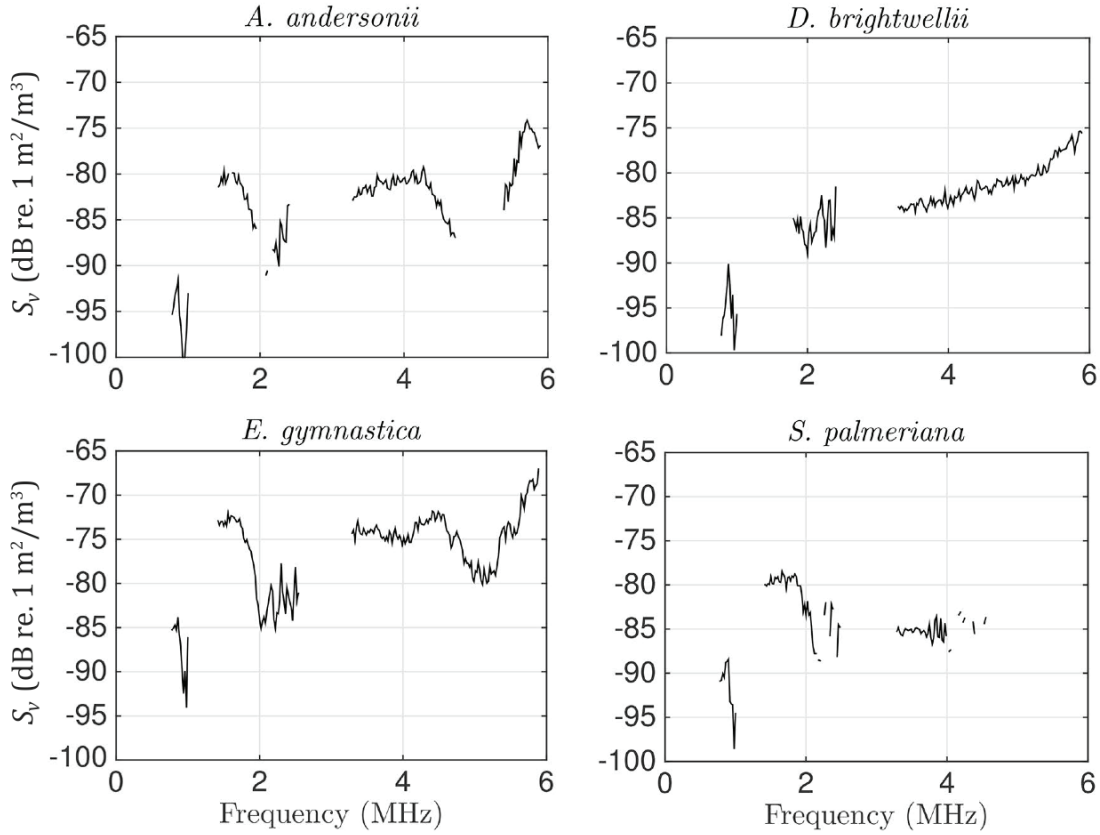


Figure 4.6: Volume scattering strengths ($S_v$) as a function of acoustic frequency for *A. andersonii*, *D. brightwellii*, *E. gymnastica*, and *S. palmeriana*. Axes limits are identical for each species to allow comparison of relative amplitudes. The gaps in the spectra are due to removal of data not exceeding the noise floor requirements as discussed in Section 3.3.5.

Volume scattering strengths ($S_v$), calculated as discussed in Section 3.3.3, are shown on a log-scale for each species in Figure 4.6 and their highest-measured concentration (their 1.0 dilution.) A log-scale is used primarily to follow convention, allowing for easier comparison to literature. For each species, $S_v$ is presented as a mean value of the 100 individual pings. Error for these results has been omitted only for clarity in reviewing the prominent features but can be seen later in Section 4.4, Figures 4.7 through 4.10. The gaps seen in the data are due to removal of data not exceeding the noise floor requirements as discussed in Section 3.3.5.

The tested species, while still large in comparison to other phytoplankton species, are still relatively small compared to the wavelengths of sound used. Recall that higher frequencies (shorter wavelengths) were originally intended in the study but these observations had to be discarded. The remaining tests were therefore done at lower $ka$ range than what would be ideal. In this lower range there is expected to be minimal distinguishing characteristics between each species' spectrum, owing to the similar backscatter returns in the *Rayleigh regime*. Only once you begin to approach $ka \sim 1$ (and $ka > 1$) are distinct characteristics expected. Here, $S_v$ takes the shape of an 'elbow-like' curve on a log-scale, between approximately -100 and -65 dB, increasing with frequency and can be generally seen in all four species with *S. palmeriana* perhaps an exception.

In what could be considered a contrast to the dilution test results, *D. brightwellii* appears to follow the expected curve. This leads me to believe that the variability in observations with respect to concentration is not owed entirely to noise but perhaps irregularity in the organism distribution (i.e. it violates the assumption of non-biased orientation and/or even distribution.) This is evaluated again in the following section.

As was already discussed when looking at the time-series for *S. palmeriana* (Section 4.1, Figure 4.4), the spectrum shows that higher frequencies ($>$ 3.00 MHz) are reduced relative to the 'elbow-like' curve shape seen for the other species. These observations in the end tend to fall very close to (and below) the observed noise floor shown in Figure 3.12. This, coupled with the dilution test series results leads me to believe that the spectrum features of *S. palmeriana* are not due to the organism's morphology and more than likely artifacts of hitting the noise floor.

A prominent feature seen in all the species except *D. brightwellii* is a relative maximum at approximately 1.5 MHz and may indicate the presence of other sources scattering within the phytoplankton system that is unaccounted for by the simple models, or by other objects entirely. One option considered and explored further in detail in Section 4.5 is that there was the presence of air pockets (i.e. bubbles), either attached to the

individual organisms or free-floating within the water column.

Lastly, both *A. andersonii* and *E. gymnastica* show a broad valley centered around 5 MHz that was not explored in any further detail, but may also represent other sources of scattering or attenuation not accounted for by the simple model. These data were not accounted for in any fitting.

## 4.4 Best-fit Models

Each species was fit against the selected models as given in Table 4.2. The root-mean-square (RMS) index was calculated for a variety of paramaterisations and the lowest RMS value is considered the most representative of the organism and termed the 'best-fit model'. The parameter range found to be the best-fit are reported alongside the model type and their respective RMS.

| | | OUTPUT | | | INPUT | | |
|---|---|---|---|---|---|---|---|
| *Species* (% of Data Fit) **Test Model** | **RMS** | $gh_{\text{fluid}}$ (min, max) | $g_{\text{fluid}}$ | $h_{\text{fluid}}$ | $g_{\text{shell}}$ | $h_{\text{shell}}$ | $v_{s,\text{shell}}$ ($\text{m}s^{-1}$) |
| *A. andersonii* (45.48) | | | | | | | |
| **EFS** | 6.66 | 1.0091 (1.0064, 1.0110) | — | — | — | — | — |
| **F-FES (I)** | 12.88 | 1.0181 (1.0082, 1.0262) | 1.0160 | 1.0021 | *1.4951* | *0.7388* | *566* |
| **F-FES (II)** | 22.14 | 1.0002 (1.0002, 1.0050) | 1.0001 | 1.0001 | *1.4951* | *2.2434* | *10* |
| **F-FES (III)** | 23.18 | 1.0002 (1.0002, 1.0051) | 1.0001 | 1.0001 | *1.4951* | *2.2434* | *40* |
| **F-FES (IV)** | 23.26 | 1.0002 (1.0002, 1.0051) | 1.0001 | 1.0001 | *1.4951* | *2.2434* | *60* |
| **F-FES (V)** | 25.07 | 1.0156 (1.0147, 1.0185) | 1.0155 | 1.0001 | *1.4951* | *2.2434* | *80* |
| *D. brightwellii* (51.60) | | | | | | | |
| **EFS** | 4.52 | 1.0015 (1.0013, 1.0018) | — | — | — | — | — |
| **F-FES** | 46.43 | 1.0002 (1.0001, 1.0230) | 1.0001 | 1.0001 | *2.1505* | *3.9289* | *3765* |
| **DWBA-Cyl** | 3.97 | 1.0016 (1.0015, 1.0018) | 1.0015 | 1.0001 | — | — | — |
| *E. gymnastica* (59.18) | | | | | | | |
| **EFS** | 7.36 | 1.0199 (1.0153, 1.0361) | — | — | — | — | — |
| **DWBA-PS** | 7.10 | 1.0281 (1.0191, 1.0403) | 1.0050 | 1.0230 | — | — | — |
| *S. palmeriana* (32.38) | | | | | | | |
| **EFS** | 8.99 | 1.0005 (1.0003, 1.0006) | — | — | — | — | — |
| **DWBA-Cyl** | 7.49 | 1.0008 (1.0003, 1.0008) | 1.0007 | 1.0001 | — | — | — |

Table 4.2: Best-fit model results for each respective species. Model abbreviations are as follows: Exact Fluid Sphere (EFS), Fluid-Filled Exact Sphere (F-FES), DWBA Cylinder (DWBA-Cyl), DWBA Prolate Sphere (DWBA-PS). The % of Data Fit is the calculated percent-ratio of dark-green to light-green solid curves seen in Figures 4.7 through 4.10. The root-mean square (RMS) value is reported as a model-fit index. The lower the RMS, the better the model fits the observed data. The $gh_{\text{fluid}}$ product is reported as a fitting parameter for the EFS models (since $g$ and $h$ cannot be separated) and as a calculated value for the others, indicated by the lighter colouring. The individually reported $g$ and $h$ for F-FES and DWBA models are the respective best-fit parameters. The columns for INPUT define the shell characteristics used in the F-FES model tests.

The best-fit models are shown plotted alongside the observed $S_v$ for each species in Figures 4.7 through 4.10. The shaded region around the mean is the error, calculated as detailed in Section 3.3.5. A dark solid line represents data that exceeds the noise, including error, and that falls within the half-max value of the calibration curve. Each species is discussed individually in the following sub-sections.

### 4.4.1 *Alexandrium andersonii*

Many comparisons were done for *A. andersonii*. While only two different theoretical models are tested, (1) the Exact Fluid Sphere (EFS) and (2) the Fluid-Filled Exact Sphere (F-FES), the F-FES models are paramaterised five different ways to give a total of 6 model fits. The different iterations of the F-FES models are described as follows.

All F-FES models assume a shell composed entirely of cellulose with a density of 1525 kg/m$^3$ (i.e. $g_{\text{shell}} = 1.4951$). This density value is equivalent to one determined for softwood cell walls (*Kellogg and Wangaard*, 1969) but is a good estimate to the generalised cellulose mechanical properties of dinoflagellate thecal plates (*Wei*, 2010; *Lau et al.*, 2007). Furthermore, if one assumes that the shell is mechanically isotropic, longitudinal and shear wave speeds can be calculated using the density ($\rho$), an elastic modulus ($E$) and Poisson ratio ($\nu$),

$$v_s = \sqrt{\frac{E}{2\rho(1+\nu)}} \tag{4.1}$$

$$v_L = \sqrt{\frac{E(1-\nu)}{\rho(1+\nu)(1-2\nu)}} \tag{4.2}$$

Setting $E = 1.3$ GPa (*Wei*, 2010), $\rho = 1525$ kg/m$^3$, and $\nu = 0.33$ (soft materials, such as cellulose, typically vary in $\nu$ from 0.3 to 0.5) the calculated shear and longitudinal wave speeds are $v_{s,\text{shell}} = 566$ m s$^{-1}$ and $v_{L,\text{shell}} = 1123$ m s$^{-1}$ (i.e. $h_{\text{shell}} = 0.7388$). It is these values that paramaterise model F-FES (I). However, while more computationally-friendly, the assumption that the shell is isotropic is likely not true considering the layered orientation of the cellulose fibrils in the thecal plates. Therefore, the remaining models II

through V explore another option in parameterisation by sourcing experimental values. In *Gadalla et al.* (2014), a longitudinal wave speed is determined from similar cell walls to be $v_{L,\text{shell}} = 3410$ m s$^{-1}$. This value is used for the remaining F-FES models. Lastly, the shear wave speed values are assumed to be similar to that of soft-body tissues and range from $v_{s,\text{shell}} = 10$ m s$^{-1}$ to $v_{s,\text{shell}} = 80$ m s$^{-1}$ (*Madsen et al.*, 1983) where each value distinguishes the remaining F-FES models.

Of these models, only the EFS (Figure 4.7) model produces a reasonably low RMS equal to 6.66. The others range from 12.88 for F-FES (I) up to a clustering of results with an RMS around 23 for the remaining models. At these frequencies, the EFS model produces a smoothly-varying spectrum. Due to the relationship of frequency and its corresponding error, the mid-frequencies likely have the largest influence on fit accuracy as they are the smoothest part of the spectrum. The anomalies in the spectrum around 1.5 MHz and 5 MHz have less of an influence. The $gh_{\text{fluid}}$ product returned for this best fit, 1.0091 with a 10% RMS variation giving a range of 1.0064 to 1.0110, is marginally biologically possible, near the minimums reported in literature for liquid and soft internal organelles (typically 1.005 - 1.1000) (*Chu and Wiebe*, 2005; *Kim et al.*, 2010; *Smith et al.*, 2013).

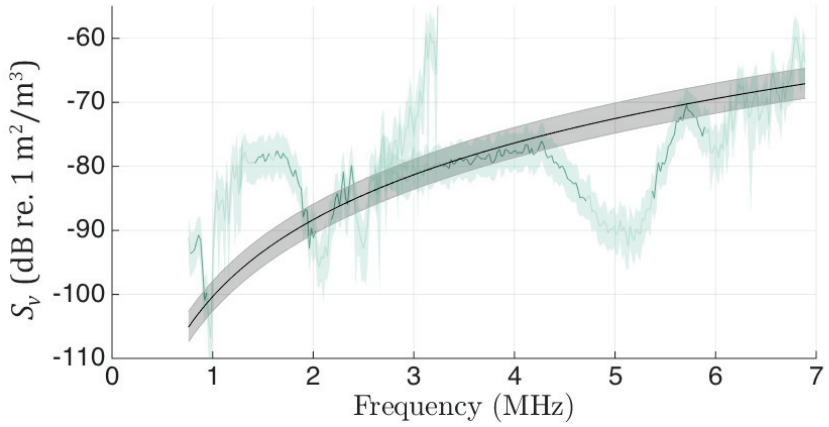


Figure 4.7: *A. andersonii* spectrum and the best model fit, EFS

Addressing the second best fit model, F-FES (I), it produces a lower RMS because

of decent correlation in the mid-frequency region (similar to the EFS model.) However, in the frequency range between 2 and 3 MHz, a large oscillatory region dominates which is not accounted for in the fitting metric due to falling in a region of excess signal to noise (i.e. rejected data.) By slightly varying the shear-wave speed, this region is shifted left or right and would, with appropriate parameterisation, fall directly on the smooth observation and result in a poor fit and high RMS. Therefore, because the shear-wave speed is not precisely known, this fit must be rejected due to the possible variability it produces.

Lastly, those of the highest RMS returns can be further disregarded as possible options once you take into account the relative $g_{\text{fluid}}$ and $h_{\text{fluid}}$ parameters for the given models. For F-FES (II) through F-FES (IV), all calculated $g_{\text{fluid}}$ and $h_{\text{fluid}}$ fall well below those expected in phytoplankton and/or zooplankton. And in the case of the F-FES (V) model, for every paramaterisation of $g_{\text{fluid}}$ and $h_{\text{fluid}}$, one value of the pair would always return as equivalent to 1.0001 (the best run is no exception, as shown in the table.)

### 4.4.2 *Diytylum brightwelii*

Three different models were tested with *D. brightwelli*: EFS, F-FES, and DWBA-Cyl. The dimensions of all models were extracted from the micrograph images. Parameterisation of the shell in the F-FES model was accomplished by assuming a silica based composition and using the corresponding acoustic parameters for silica ($g_{\text{shell}} = 2.15$, $h_{\text{shell}} = 3.93$ compared to seawater and $c_s = 3700$ m s$^{-1}$ (*Lide*, 2005).)

Ultimately, two of the three fits performed well (the best amongst all the species, in fact). The DWBA-Cyl fit outperformed the EFS fit with an RMS value of 3.97 compared to 4.52 respectively. However, as was seen in the case of the poor performing models of *A. andersonii*, the $g_{\text{fluid}}$ and $h_{\text{fluid}}$ returned for these two reasonable fits were below those regularly seen in previous studies. Additionally, of any of the species studied, *D. brightwellii* was the most likely to be represented by a shelled-model, or similarly, by a biased-high $g_{\text{fluid}}$ and $h_{\text{fluid}}$ fluid-model as used in previous studies (*Holliday et al.*, 1979; *Kim et al.*, 2010). The fitted results do not support this at all and coupled with the dilution

test series, this is further evidence that *D. brightwelii* was not observed accurately in the study.

A possible reason for the reduced scatter is similar to the explanation given in Section 4.1 for *S. palmeriana*. That is to say, the assumption of even distribution and random orientation of the individual organisms was violated in this experiment (as already mentioned, perhaps due to the latent vorticity in the tank following mixing in between insonofication tests.) However, there is no way to test this possibility and so it is left as an option for future study.

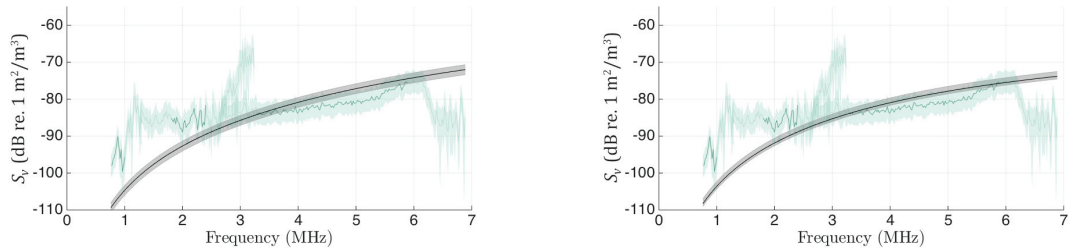


(a) EFS (b) DWBA-Cyl

Figure 4.8: *D. brightwellii* spectra and the two best model fits.

### 4.4.3 *Eutreptiella gymnastica*

Both models tested, EFS and DWBA-PS, produced statistically equivalent (according to the bootstrap analysis) RMS values of 7.36 and 7.10 respectively. Of the species tested (excluding *S. palmeriana* for reasons discussed in the following sections) these were the highest RMS values returned. However, while high, they still fall within 10% of the lowest RMS values that were returned for *A. andersonii*. From the dilution tests (Section 4.2), *E. gymnastica* appears to be a a well sampled species as is suggested by the matched decrease in scattering intensity and concentration. Additionally, the acoustic parameters $g_{\text{fluid}}$ and $h_{\text{fluid}}$ returned from the models are biologically consistent with previous studies, coming in at the lower bound similar to the *A. andersonii* test. For the EFS model, a $gh_{\text{fluid}}$ product of 1.0199 was returned for the best fit and a range between 1.0153 to 1.0361 was determined corresponding to the allowable 10% variation in the RMS. Likewise, for the

prolate spheroid model, a $gh_{\text{fluid}}$ product of 1.0281($g_{\text{fluid}}$ = 1.0050, $h_{\text{fluid}}$ = 1.0230) was returned with a range between 1.0191 and 1.0403.

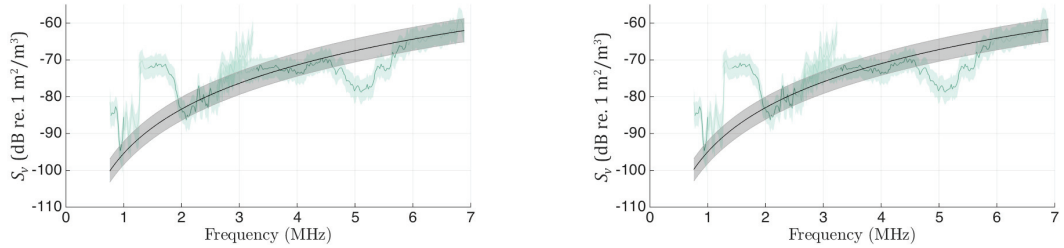


(a) EFS (b) DWBA-PS

Figure 4.9: *E. gymnastica* spectra and the two best model fits.

### 4.4.4 *Stephanopyxis palmeriana*

*Stephanopyxis palmeriana* was the fourth species tested in this study. It is a prolific chain-former and was observed to have on average 4 or more individual cell units making up each chain. These long chain lengths gave it the highest length-to-width ratio of any species studied. Being fairly large, even as individual cells, and of comparable concentration to the higher dilutions of both *A. andersonii* and *E. gymnastica*, originally led me to expect high to very high scattering returns. Instead, I observed a comparatively weak signal across the bandwidth with the majority of the signal falling below the set noise threshold. Ultimately, only 32.38% of the observed scattering spectrum was strong enough to be used for fitting, the lowest of all the species.

Nevertheless, a comparison was still performed for two models: EFS and DWBA-Cyl. The DWBA-Cyl result (see Figure 4.10) returned the lower RMS of 7.49. Composition values returned for this model are $g_{\text{fluid}} = 1.0007$ and $h_{\text{fluid}} = 1.0001$. Both of these values fall below expected biological values for phytoplankton, shell or not. This result reconfirms the previous suggestion that *S. palmeriana* was below a detectable limit.

One possible explanation for the unexpectedly low scatter is inaccuracies in the concentration measurements. Recall that for this species a haemocytometer was used to calculate concentration. Being such a large organism, very few individual chains could

be counted (at times only 1 or 2) within the measurement grid of the instrument and introduced a comparatively large error to those obtained with a flow cytometer. If the concentration observed by this method exceeded that of the actual culture, it would force the model fits to produce lower than expected $g_{\text{fluid}}$ and $h_{\text{fluid}}$. However, there is no reason to believe that the method would bias the concentration estimate high. Therefore, if an alternative method were to be used to calculate concentration with more accuracy, a more definitive conclusion could be made.

Another possible explanation, already discussed at the beginning of Section 4.1, is that the organisms may have not been oriented randomly within the water column. A scattering decrease would occur if the narrow-edges of the chains were angled toward the transducers. However, there is no way to test this possibility and so it is left as an option for future study.

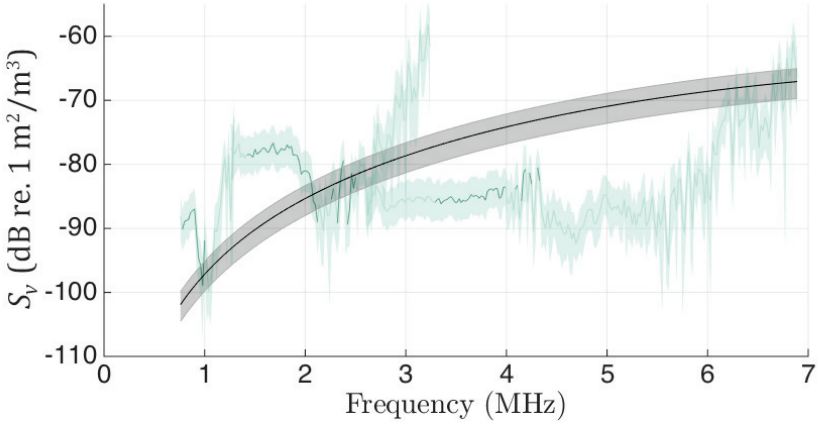


Figure 4.10: *S. palmeriana* spectra and the best model fit, DWBA-Cyl.

## 4.5 Possible Bubble Scattering

As was discussed earlier, three of the species were observed to have an apparent resonance around 1.5 MHz. The $S_v$ in this region rises up to 20 dB higher than suggested by any of the models considered here. The resonance is also fairly broad, spanning approximately 1 MHz. One possible explanation of the resonance is scattering from a distribution of

microbubbles, either attached to the organisms or freely floating within the water column. To test this possibility, an air-filled spherical (i.e. bubble) model (*Medwin and Clay*, 1998) is fit against the *A. andersonii* for a distribution of microbubbles and paramaterised to find a concentration. The radii of the bubbles, $a$, are calculated from the breathing frequency of bubbles at a depth of 0 metres (*Medwin and Clay*, 1998),

$$f_b = \frac{3.25 \times 10^6}{a} \tag{4.3}$$

where $f_b$ is set to a normal distribution ($N_{count} = 1000$ ) of frequencies of $1.54 \pm 0.19$ MHz. This produces a range of radii of $2.12 \pm 0.56\mu$m.

Performing the fit (Figure 4.11), it is found that a concentration of just 7.0 bubbles/m$^3$ is required to match the resonance peak values seen in the observations. This result is incredibly low and can therefore likely be discredited as the contributing factor to the localised increase in $S_v$. In particular, this feature is seen uniformly ping-to-ping in the observations. If a concentration of just 7.0 bubbles/m$^3$ is to be believed, and given that the insonification volume was on the order of $10^{-5}$ m$^3$, there would need to be far less than 1 bubble in the insonification volume. Additionally, there would have needed to be consistently $7 \times 10^{-5}$ bubbles present to produce the uniform observations seen over the 100 individual pings.

Therefore, it remains that the observed peak in the $S_v$ must be related to morphological contributions to the scattering or an error in calibration (unlikely due to the lack of appearance in *D. brightwellii* observations) or unknown variations in the experimental setup. The possibility of an unintentional change of experimental setup is increasingly more likely when reviewing the background signal in Figure 3.12. Here, the feature is clearly visible in background with similar amplitude. While extreme care was taken to not shift the transducer angle between experiments, it is certainly possible that such an alteration did occur. However, no tests precede *D. brightwellii* and so this cannot be explored any further, however likely it is.

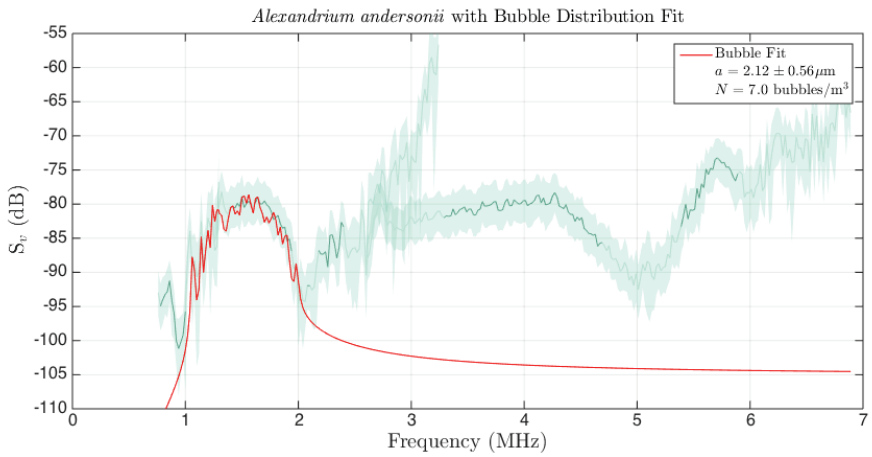


Figure 4.11: .
Bubble model fit (red) over spectral feature in *A. andersonii* volume scattering strength. Bubble radii are set to a normal distribution of $2.12 \pm 0.56\mu$m. The fit returned a concentration value of N = 7.0 bubbles/m$^3$.

# CHAPTER 5

# CONCLUSIONS

A high-frequency broadband acoustic system was developed and used to insonify the unique test environment required by the mono-cultures of phytoplankton. Unforeseen instrumental limitations reduced the intended frequency range of the study, but the system was still capable of measuring across 0.75 to 6.90 MHz.

Four species of morphologically distinct phytoplankton were successfully grown to high concentrations: (1) *Alexandrium andersonii*, (2) *Ditylum brightwellii*, (3) *Eutreptiella gymnastica*, and (4) *Stephanopyxis palmeriana*. Even though the species were grown to high concentrations, their backscatter was still quite low due to their composition and relative acoustic characteristics; i.e. they are weak scatterers. To maximize the detection of the signal, pulse compression and band-pass filtering were applied and background noise and calibration carefully considered. Despite these efforts, two species, *D. brightwellii* and *S. palmeriana*, still proved difficult to accurately detect even at the highest concentrations, likely due to their detection being below the noise floor. However, as indicated by the $S_v$ results, *D. brightwelii* may owe its variability to not just noise, but also variability of the organisms (e.g. faster settling or biased orientation) in the scattering region, thereby violating assumptions made in the modelling process. The other two species were measured with confidence, including at decreasing concentrations (fulfilling Objectives 1 and 2 of this thesis). Both *A. andersonii* and *E. gymnastica* were detected down to concentrations

of at least $2.794 \times 10^9$ individuals/m$^3$ and $8.061 \times 10^8$ individuals/m$^3$, respectively with frequencies of $1.25\,\mathrm{MHz}$ up to $6.90\,\mathrm{MHz}$. Additionally, these abundance levels are similar to those measured in the field (*Smayda*, 1997). Because detection limit is affected by both the limitations of instrumentation and the scattering characteristics of the species, this part of the study was conducted such that the subsequent frequency analysis, which considered only the highest concentrations of phytoplankton, could be applied with confidence.

Spectra of the volume scattering strength were used to examine the scattering frequency response of each species. The $S_v$ spectrum took the form of an 'elbow-like' curve on the log-scale while increasing with frequency. *Stephanopyxis palmeriana* was an exception due to the limited data that exceeded the background noise. The increase in scattering amplitude with frequency is typical in the Rayleigh scattering regime and reaffirms that the mono-cultures were being observed acoustically. Additionally, the species indeed do have different spectra. However, given the fact that most of these data were collected in the Rayleigh regime, these species-unique features are not likely caused by morphological differences. A prominent feature seen in 3 of the species was initially considered to be the influence of bubbles within the tank but upon calculation, it seems improbable given the low bubble concentrations required.

Each species was modeled by at least two scattering models with each including representation by a fluid-filled sphere model; as is common in current phytoplankton scattering literature. A root-mean-squared variance for each model was used to determine a best-fit model. From the best-fit, the paramaterisation of density ($g_{\text{fluid}}$) and sound-speed ($h_{\text{fluid}}$) contrasts are presented.

The models used for *Alexandrium andersonii* included five uniquely-parameterised shell models alongside the fluid-sphere model. It was determined that the exact fluid-filled sphere model performed best, giving an best-fit RMS value of 6.66 and an acoustic parameter $gh_{\text{fluid}}$ of 1.0091 with the 10% RMS variation giving a range of 1.0064 to 1.0110. These values conform to previously reported values seen in literature for liquid

and soft internal organelles (typically 1.005 - 1.1000) (*Chu and Wiebe*, 2005; *Kim et al.*, 2010; *Smith et al.*, 2013). Therefore, an exact fluid-filled sphere model is likely the most appropriate to model this species at these frequencies.

*Ditylum brightwellii* observations were compared to a DWBA cylindrical model and a fluid-filled elastic shell model in addition to the exact fluid-filled sphere. The DWBA cylindrical model and the exact fluid-filled sphere model were determined to be the best fits, with RMS values of 3.97 and 4.52 respectively. However, the acoustic parameters returned for these fits fell below those regularly reported in literature. Additionally, variation in scattering intensity was observed in this species when conducting the dilution tests. These results together may suggest that while the species was detected above the noise threshold, that it was not modelled correctly, namely due to assumptions of even distribution and non-biased orientation being violated. Therefore, no suggestions can be made following this study as to how to best model their scatter. Further study is necessary to see if the assumptions are indeed being violated – perhaps via optical methods.

For *Eutreptiella gymnastica*, I considered two model candidates, the exact fluid-filled sphere and a DWBA prolate spheroid. Both performed similarly, producing statistically equivalent RMS values of 7.36 and 7.10 respectively. For the exact fluid-filled sphere model, a $gh_{\text{fluid}}$ product of 1.0199 was returned for the best fit and a range between 1.0153 to 1.0361 was determined corresponding to the allowable 10% variation in the RMS. Likewise, for the DWBA-PS model, a $gh_{\text{fluid}}$ product of 1.0281($g_{\text{fluid}}$ = 1.0050, $h_{\text{fluid}}$ = 1.0230) was returned with a range between 1.0191 and 1.0403. Like *A. andersonii*, these acoustic parameters are within the ranges reported in previous studies. A large portion of the range of fitted parameters is shared between the two models. However, the DWBA prolate spheroid does produce, on average, slightly higher parameters. This can be attributed to its higher length-to-width ratio. And so, while at these lower $ka$ ranges the distinction is less important, it may become essential at higher frequencies to consider a prolate sphere model. This becomes more important as the length-to-width ratio of any

measured species increases. As for the frequencies used in this study, there is limited improvement in using a prolate sphere and a simple exact fluid-filled sphere model is sufficiently accurate to model this species and similar morphologies.

*Stephanopyxis palmeriana* proved to be the most challenging species to detect. The majority of the spectrum of *S. palmeriana* was below the noise floor and so only about 32% of the data were available to compare with the scattering models, with most of it being in the lower part of the bandwidth. Of the models tested, the DWBA fluid cylinder model scored best and returned a very low $gh_{\text{fluid}}$ equal to 1.0001. Even for a weakly scattering organism, this $gh$ product, is well below those previously seen in studies. It is likely that the majority of the observations this species was at the noise floor. This could be due to invalidated assumptions including non-uniform distribution or orientation bias, or poor methods in determining its concentration. Therefore, no recommendation can be made for an appropriate model choice of this species at the studied frequencies.

The spectral analysis of the scattering from these four species satisfies the fourth goal of this thesis. In addition, recommendations have been made for two of the species for which models would best approximate them at frequencies between 0.75 and 6.90 MHz. While this is the first work to test different models, these recommendations support the methods in use in the few phytoplankton scattering papers published to date. It is likely that for organisms of this size, and at these frequencies, alternative models to the fluid-filled sphere offer little to no improvement.

The final question this thesis intended to address is if a high-frequency broadband acoustic system is appropriate for remote sensing subsurface HABs. Reading recent publications (*Kim et al.*, 2018), it is clear that groups have developed and deployed such devices capable of detecting phytoplankton in the open ocean. However, a larger part of the question relates to the differentiation of species. As this thesis has shown, it is indeed possible to observe phytoplankton, even to small length scales, provided that you use high enough frequencies. It is unlikely though, that species differentiation would be possible

acoustically for frequencies below 7 MHz. However, one must consider the trade-off of range going to higher frequencies–as you begin to exceed 20 MHz, you will begin to range-limit appropriately powered sonar systems (i.e. systems not prone to produce cavitation, streaming, etc) to centimeters. And, even with perfectly resolved very high-frequency spectra, it would be difficult given the diversity of species typically present in the ocean. In the context of monitoring HABs, if a singular species is known to inhabit a region, it could be monitored with a single frequency. Additionally, if there were very few species, sufficiently different in size, that dominated the phytoplankton assemblage, broadband acoustics might be able to distinguish them. However, as discussed in the recent *Kim et al.* (2018) paper, species may behave differently in the ocean versus a lab tank. These peculiarities would need to be identified for any particular species and for any particular environment before such a system could be utilized accurately.

## 5.1 Recommendations for Future Work

A primary motivation of this thesis was to explore the option of differentiating species using an acoustic system. The inability of the work shown in this thesis to show this conclusively, motivates the majority of this future work section. In particular, the frequencies were capped at $6.9\,\mathrm{MHz}$ once the $10\,\mathrm{MHz}$ transducer proved unusable. The first recommendation would be to employ higher frequencies. Increasing the operational frequencies to 10-15 MHz would push the $ka$ range of the studied species past the Rayleigh regime into a transitional one. At these $ka$ values, predicted scattering from the models described in this thesis begin to diverge more drastically and would provide a greater chance at differentiating spectra.

Another challenge in this study was the persistent low signal-to-noise ratio. Efforts were made to mitigate this problem, but there were limitations in the system preventing other opportunities such as the use of desktop computer PCIe peripherals for the generation and digitization of signals. Moving to separate, purpose-built instrumentation might

provide more opportunity to amplify the transmission and reception of signals and would be worth looking into for future work.

Lastly, when designing the acoustic apparatus, freedom of movement (linearly as well as rotationally) was intentionally included. This design feature may have proved to be problematic and possibly explaining the lack of a $1.5\,\mathrm{MHz}$ feature in the observed volume scattering strength of *D. brightwellii*. If a future system were to be designed for use in laboratory experiments, I would suggest to keep the components stationary to remove as much movement as possible and to remove one possible source of error.

# BIBLIOGRAPHY


Algae Resource Database, *Microcystis aeruginosa* strain no. NIES-102. Online, http://www.shigen.nig.ac.jp/algae/strainDetailAction.do?stockNo=NIES-102, Accessed: 2015-06-26.

Anderson, D. M., T. J. Alpermann, A. D. Cembella, Y. Collos, E. Masseret, and M. Montresor, The globally distributed genus *Alexandrium*: multifaceted roles in marine ecosystems and impacts on human health, *Harmful Algae*, *14*, 10–35, 2012.

Anderson, V., Sound scattering from a fluid sphere, *Journal of the Acoustical Society of America*, *20*, 426–431, 1950.

Blanc, S., C. E. Bentez, M. I. E. de Milou, P. Mosto, G. Lascalea, and R. Jurez, Acoustical behaviour of phytoplanktonic algae, *Acoustics Letters*, *23*, 175–183, 2000.

Brand, L. E., R. R. L. Guillard, and L. S. Murphy, A method for the rapid and precise determination of acclimated phytoplankton reproduction rates, *Journal of Plankton Research*, *3*, 193–201, 1981.

Chu, D., and T. K. Stanton, Application of pulse compression techniques to broadband acoustic scattering by live individual zooplankton, *Journal of the Acoustical Society of America*, *104*, 39–55, 1998.

Chu, D., and P. H. Wiebe, Measurements of sound-speed and density contrasts of zooplankton in antarctic waters, *ICES Journal of Marine Science*, *62*, 818–831, 2005.

Cloern, J. E., Our evolving conceptual model of the coastal eutrophication problem, *Marine Ecology Progress Series*, *210*, 223–253, 2001.

Conley, D. J., Biogeochemical nutrient cycles and nutrient management strategies, *Hydrobiologia*, *419*, 87–96, 2000.

Cupp, E. E., *Marine Plankton Diatoms of the West Coast of North America*, University of California Press, Berkley, California, 1943.

Dourado, N., Sediment laden ice detection using broadband acoustic backscattering measurements from calibration targets in ice, Master's thesis, Dalhousie University, Halifax, N.S., Canada, 2015.

Efron, B., and G. Gong, A leisurely look at the bootstrap, the jackknife, and cross-validation, *The American Statistician*, *37*, 36–48, 1983.

EOL - Encyclopedia of Life, *Alexandrium fundyense*. Online, http://www.eol.org/pages/910093/overview, Accessed: 2017-01-14.

Francois, R. E., and G. R. Garrison, Sound absorption based on ocean measurements: Part ii:boric acid contribution and equation for total absorption, *Journal of the Acoustical Society of America*, *72*, 1982.

Gadalla, A., T. Dehoux, and B. Audoin, Transverse mechanical properties of cell walls of single living plant cells probed by lasergenerated acoustic waves, *Planta*, *239*, 1129, 2014.

Gaunaurd, G. C., and M. F. Werby, Lamb and creeping waves around submerged spherical shells resonantly excited by sound scattering, *Journal of the Acoustical Society of America*, *82*, 1987.

Goodman, R. R., Reflection and transmission of sound by elastic spherical shells, *Journal of the Acoustical Society of America*, *34*, 338–344, 1962.

Greenlaw, C. F., Acoustical estimation of zooplankton populations, *Limnology and Oceanography*, *24*, 226–242, 1979.

Guillard, R. R. L., *Methods for microflagellates and nanoplankton. In: Stein, J.R. (ed) Handbook of Phycological Methods - Culture Methods and Growth Measurements*, Cambridge University Press, Cambridge, 1973.

Guillard, R. R. L., *Culture of phytoplankton for feeding marine invertebrates. In: Smith, W. L. and Chanley M. H. (eds) Culture of marine invertebrate animals*, Plenum, New York, NY, 1975.

Guillard, R. R. L., and P. E. Hargraves, *Stichochrysis immobilis* is a diatom, not a chrysophyte, *Phycologia*, *32*, 234–236, 1993.

Hasle, G. R., and E. E. Syvertsen, *Marine diatoms. - In: Tomas, C. R. (ed.): Identifying Marine Phytoplankton*, Academic Press, San Diego, CA, 1997.

Holliday, D. V., R. E. Pieper, and G. S. Kleppel, Determination of zooplankton size and distribution with multifrequency acoustic technology, *ICES Journal of Marine Science*, *46*, 52–61, 1979.

Johnson, R. K., Sound scattering from a fluid sphere revisited, *Journal of the Acoustical Society of America*, *61*, 375–377, 1977.

Kellogg, R. M., and F. F. Wangaard, Variation in the cell-wall density of wood, *Wood and Fiber Science*, *3*, 1969.

Kim, E., L. Hyungbeen, N. Jungyal, J. W. Choi, and D. Kang, 5-MHz acoustic-backscatter measurements of *Cochlodinium polykrikoides* blooms in Korean coastal waters, *ICES Journal of Marine Sciences*, *67*, 1759–1765, 2010.

Kim, H., T. H. Bok, D. G. Paeng, J. Kim, K. H. Nam, J. B. Lee, and M. M. R. Shah, Mobility of *Amphidinium carterae* Hulburt measured by high-frequency ultrasound, *Journal of the Acoustical Society of America*, *141*, EL395, 2017.

Kim, H., D. Kang, and S. W. Jung, Development and application of an acoustic system for harmful algal blooms (habs, red tide) detection using an ultrasonic digital sensor, *Ocean Science Journal*, *53*, 91–99, 2018.

Kristensen, A., and J. Dalen, Acoustic estimation of size distribution and abundance of zooplankton, *Journal of the Acoustical Society of America*, *80*, 601–611, 1986.

Lau, R. K., A. C. Kwok, W. K. Chan, T. Y. Zhang, and J. T. Wong, Mechanical characterization of cellulosic thecal plates in dinoflagellates by nanoindentation, *Journal of Nanoscience and Nanotechnology*, *7*, 452–457, 2007.

Lavery, A., and T. Ross, Acoustic scattering from double-diffusive microstructure, *Journal of the Acoustical Society of America*, *122*, 1449–1462, 2007.

Lavery, A., P. H. Wiebe, T. K. Stanton, G. L. Lawson, M. C. Benfield, and N. Copley, Determining dominant scatterers of sound in mixed zooplankton populations, *Journal of the Acoustical Society of America*, *122*, 3304–3326, 2007.

Lavery, A., D. Chu, and J. Moum, Measurements of acoustic scattering from zooplankton and oceanic microstructure using a broadband echosounder, *ICES Journal of Marine Science*, *67*, 379–394, 2009.

Lide, D. R., *Table 1: "Speed of Sound in Solids at Room Temperature" in CRC Handbook of Chemistry and Physics*, CRC Press, Boca Raton, FL, 2005.

MacIntyre, H. L., and J. J. Cullen, Classifications of phytoplankton cells as live or dead using the vital stains fluorescein diacetate and 5-chloromethylfluorescein diacetate, *Journal of Phycology*, *52*, 572–589, 2016.

MacIntyre, H. L., J. J. Cullen, T. J. Whitsitt, and B. Petri, Enumerating viable phytoplankton using a culture-based most probably number assay following ultraviolet-c treatment, *Journal of Applied Phycology*, *30*, 1073–1094, 2018.

Madsen, E., J. Sathoff, and J. Zagzebski, Ultrasonic shear wave properties of soft tissues and tissuelike materials, *Journal of the Acoustical Society of America*, *74*, 1346, 1983.

Martin, L. V., T. K. Stanton, P. H. Wiebe, and J. Lynch, Acoustic classification of zooplankton, *ICES Journal of Marine Science*, *53*, 217–224, 1996.

Medwin, H., and C. S. Clay, *Fundamentals of Acoustical Oceanography*, Academic Press, San Diego California, 1998.

Morse, P. M., and K. U. Ingard, *Theoretical Acoustics*, Princeton University Press, Princeton, New Jersey, 1968.

NASA Earth Observatory, Algae bloom in lake erie. Online, `http://earthobservatory.nasa.gov/IOTD/view.php?id=76127`, Accessed: 2015-06-26.

Paerl, H., L. Valdes-Weaver, A. Joyner, and V. Winkelmann, Phytoplankton indicators of ecological change in the eutrophying Pamlico Sound system, North Carolina, *Ecological Applications*, *17*, S88–S101, 2007.

Platt, T., and S. Sathyendranath, Ecological indicators for the pelagic zone of the ocean from remote sensing, *Remote Sensing of Environment*, *112*, 3426–3436, 2008.

Rabalais, N., and R. Turner, Coastal hypoxia: Consequences for living resources and ecosystems, *Coastal and Estuarine Studies*, *58*, 2001.

Rabalais, N., R. Turner, R. Diaz, and D. Justic, Global change and eutrophication of coastal waters, *ICES Journal of Marine Science*, *66*, 1528–1537, 2009.

Ross, T., and R. Lueck, Sound scattering from oceanic turbulence, *Geophysical Research Letters*, *30*, 1344–1348, 2003.

Round, F. E., R. M. Crawford, and D. G. Mann, *The Diatoms*, Cambridge University Press, Cambridge, 1990.

Selivanovsky, D. A., P. A. Stunzhas, and I. N. Didenkulov, Acoustical investigation of phytoplankton, *ICES Journal of Marine Science*, *53*, 313–316, 1996.

Shoaf, W. T., and B. W. Lium, Improved extraction of chlorophyll *a* and *b* from algae using dimethyl sulfoxide, *Limnology and Oceanography*, *21*, 926–928, 1976.

Smayda, T. J., What is a bloom? A commentary, *Limnology and Oceanography*, *42*, 1132–1136, 1997.

Smith, J. N., P. H. Ressler, and J. D. Warren, A distorted wave born approximation target strength model for bering sea euphausiids, *ICES Journal of Marine Science*, *70*, 204–214, 2013.

Smithsonian Institute, Indian River Lagoon Species Inventory: *Ditylum brightwellii*. Online, `http://www.sms.si.edu/irlspec/Ditylu_bright.htm`, Accessed: 2016-09-29.

Stanton, T., R. Nash, R. Eastwood, and R. Nero, A field examination of acoustical scattering from marine organisms at 70 kHz, *IEEE Journal of Oceanic Engineering*, *12*, 339–348, 1987.

Stanton, T. K., Simple approximate formulas for backscattering of sound by spherical and elongated objects, *Journal of the Acoustical Society of America*, *86*, 1499–1510, 1989.

Stanton, T. K., and D. Chu, Calibration of broadband active acoustic systems using a single standard spherical target, *Journal of the Acoustical Society of America*, *124*, 128–136, 2008.

Stanton, T. K., H. Wiebe, D. Chu, M. C. Benfield, L. Scanlon, L. Martin, and R. L. Eastwood, On acoustic estimates of zooplankton biomass, *ICES Journal of Marine Sciences*, *51*, 505–512, 1994.

Stanton, T. K., D. Chu, and P. Wiebe, Acoustic scattering characteristics of several zooplankton, *ICES Journal of Marine Sciences*, *53*, 289–295, 1996.

Stanton, T. K., D. Chu, P. Wiebe, L. Martin, and R. L. Eastwood, Sound scattering by several zooplankton groups. I. Experimental determination of dominant scattering mechanisms, *Journal of the Acoustical Society of America*, *103*, 225–235, 1998a.

Stanton, T. K., D. Chu, P. Wiebe, L. Martin, and R. L. Eastwood, Sound scattering by several zooplankton groups. II. Scattering models, *Journal of the Acoustical Society of America*, *103*, 236–253, 1998b.

Stanton, T. K., D. Chu, P. H. Wiebe, R. L. Eastwood, and J. D. Warren, Acoustic scattering by benthic and planktonic shelled animals, *Journal of the Acoustical Society of America*, *108*, 535–550, 2000.

Throndsen, J., Flagellates of Norwegian coastal waters, *Norwegian Journal of Botony*, *16*, 161–216, 1969.

USCS Ocean Data Center, *Stephanopyxis palmeriana*. Online, `http://oceandatacenter.ucsc.edu/PhytoGallery/Diatoms/stephanopyxis.html`, Accessed: 2014-01-14.

Wei, Y., Characterization of cellulosic thecal plates of dinoflagellates, Master's thesis, Hong Kong University of Science and Technology, Hong Kong, 2010.

Welschmeyer, N. A., Fluorometric analysis of chlorophyll *a* in the presence of chlorophyll *b* and pheopigments, *Limnology and Oceanography*, *39*, 1985–1992, 1994.